

1 **Phospholipase D3 contributes to Alzheimer's disease risk via disruption of A $\beta$  clearance**  
2 **and microglia response to amyloid plaques**

3  
4 Matthew J. Rosene<sup>1</sup>, Simon Hsu<sup>1</sup>, Shih Feng You<sup>1</sup>, Logan Brase<sup>1</sup>, Anthony Verbeck<sup>1</sup>, Rita  
5 Martinez<sup>1</sup>, Clare E. Wallace<sup>2,7</sup>, Zeran Li<sup>1</sup>, Ping Yan<sup>2</sup>, Nina M. Dräger<sup>3,4</sup>, Sydney M. Sattler<sup>3,4</sup>,  
6 Abhirami K Iyer<sup>1</sup>, Shannon L Macauley<sup>5,6</sup>, David M. Holtzman<sup>2,7</sup>, Bruno A. Benitez<sup>1,7</sup>, Martin  
7 Kampmann<sup>3,4</sup>, Carlos Cruchaga<sup>1,7</sup>, Oscar Harari<sup>1,7</sup>, John R. Cirrito<sup>2,7</sup>, Jin-Moo Lee<sup>2,7</sup>, Alison M.  
8 Goate<sup>8,9</sup>, Celeste M. Karch<sup>1,7\*</sup>

9  
10 Affiliations:

11 <sup>1</sup>Department of Psychiatry, Washington University, St. Louis, MO 63110, USA

12 <sup>2</sup>Department of Neurology, Washington University, St. Louis, MO 63110, USA

13 <sup>3</sup>Department of Biochemistry and Biophysics, University of California, San Francisco, San  
14 Francisco, CA, USA

15  
16 <sup>4</sup>Institute for Neurodegenerative Diseases, University of California, San Francisco, San  
17 Francisco, CA, USA

18  
19 <sup>5</sup>Department of Internal Medicine, Section on Gerontology and Geriatric Medicine, Wake Forest  
20 School of Medicine, Winston-Salem, North Carolina, USA.

21  
22 <sup>6</sup>Wake Forest Alzheimer's Disease Research Center, Wake Forest School of Medicine,  
23 Winston-Salem, North Carolina, USA.

24  
25 <sup>7</sup>Hope Center for Neurological Disorders, St. Louis, MO 63110, USA

26 <sup>8</sup>Department of Genetics and Genomic Sciences, Icahn Institute of Genomics and Multiscale  
27 Biology, Icahn School of Medicine at Mount Sinai, New York, NY, USA.

28  
29 <sup>9</sup>Ronald M. Loeb Center for Alzheimer's Disease, Icahn School of Medicine at Mount Sinai, New  
30 York, NY, USA.

31  
32  
33 **Corresponding Author:** Celeste M. Karch, Department of Psychiatry, Washington University  
34 School of Medicine, 425 S. Euclid Ave, Campus Box 8134, St. Louis, MO 63110, phone: 314-  
35 747-3161, fax: 314-747-2983, email: [karchc@wustl.edu](mailto:karchc@wustl.edu)

36 **Abstract**

37  
38 Alzheimer's disease (AD) is characterized by the accumulation of amyloid- $\beta$  (A $\beta$ ) plaques and  
39 neurofibrillary tangles in the brain. AD is also the result of complex genetic architecture that can  
40 be leveraged to understand pathways central to disease processes. We have previously  
41 identified coding variants in the *phospholipase D3* (*PLD3*) gene that double the late-onset AD  
42 risk. However, the mechanism by which *PLD3* impacts AD risk is unknown. One AD risk variant,  
43 *PLD3* p.A442A, disrupts a splicing enhancer-binding site and reduces *PLD3* splicing in human  
44 brains. Using differentiated induced pluripotent stem cells from a *PLD3* p.A442A carrier and  
45 CRISPR-reverted, isogenic control, we show that *PLD3* p.A442A cortical neurons exhibit a  
46 *PLD3* splicing defect and a significant increase in A $\beta$ 42 and A $\beta$ 40, both of which are corrected  
47 upon reversion of the risk allele in isogenic control neurons. Thus, *PLD3* p.A442A is sufficient to  
48 alter *PLD3* splicing and A $\beta$  metabolism. While the normal function of *PLD3* is poorly understood,  
49 *PLD3* is highly expressed in neurons and brain regions most susceptible to amyloid pathology.  
50 *PLD3* expression is significantly lower in AD brains than controls, suggesting that *PLD3* may  
51 play a role in sporadic AD. Thus, we sought to determine whether *PLD3* contributes to A $\beta$   
52 accumulation in AD. In a mouse model of amyloid accumulation, loss of *Pld3* increases  
53 interstitial fluid (ISF) A $\beta$  and reduces A $\beta$  turnover. AAV-mediated overexpression of *PLD3* in the  
54 hippocampus decreased ISF A $\beta$  levels and accelerated A $\beta$  turnover. To determine whether  
55 *PLD3*-mediated reduction of ISF A $\beta$  impacts amyloid accumulation, we measured amyloid  
56 plaque abundance and size after significant A $\beta$  deposition. We found that in the absence of  
57 *Pld3*, amyloid plaques were less compact and more diffuse. Additionally, we observed reduced  
58 recruitment of microglia to amyloid plaques in the absence of *Pld3*. *PLD3* may impact amyloid  
59 accumulation and AD risk through disrupted microglia function as *PLD3* is enriched in disease  
60 associated microglia in human brains. Together, our findings demonstrate that *PLD3* regulates

61 A $\beta$  clearance through cell-autonomous and non-cell-autonomous pathways in a manner that  
62 likely contributes to AD risk.

63  
64  
65

## 66 Introduction

67  
68 Alzheimer's disease (AD) is pathologically defined by neuronal loss and the  
69 accumulation of amyloid- $\beta$  (A $\beta$ ) plaques and neurofibrillary tangles in the brain. Genetic,  
70 biochemical, and neuropathologic data suggest that A $\beta$  aggregation is central to initiating AD  
71 pathogenesis [1]. Rare mutations in *APP*, *PSEN1*, and *PSEN2* cause dominantly inherited AD.  
72 Late-onset AD (LOAD) also has a strong genetic component [2]. Identifying novel loci that affect  
73 LOAD risk is critical to our understanding of the underlying etiology of AD and novel therapeutic  
74 pathways.

75 The genetic architecture that underlies LOAD is complex [2]. Large-scale genomic  
76 studies have led to the identification of novel genes and risk loci that contribute to AD [2, 3].  
77 Whole exome sequencing of densely affected LOAD families has revealed a rare genetic variant  
78 within *PLD3* (p.V232M) that perfectly segregated with disease in two independent families and  
79 doubled AD risk in seven independent case-control series (4,998 AD cases/6,356 controls;  
80 OR=2.10,  $p=2.93 \times 10^{-5}$ ) [4]. Gene-based analyses indicated that multiple variants in *PLD3*  
81 increase AD risk in European (EA) and African American (AA) populations (e.g.: p.M6R,  
82 p.V232M, p.A442A; EA: OR=2.75,  $p=1.44 \times 10^{-11}$ ; AA: OR=5.48,  $p=1.40 \times 10^{-3}$ ) [4].

83 *PLD3* is a non-classical member of the phospholipase D (PLD) family of enzymes, with  
84 no known function [5-7]. *PLD3* is expressed in pyramidal neurons within the brain, and in AD  
85 brains, *PLD3* co-localizes with amyloid plaques [8, 9]. Common variants in *PLD3* are associated  
86 with CSF A $\beta$  levels, an AD biomarker [10]. *In vitro*, *PLD3* expression is correlated with  
87 extracellular A $\beta$  levels: *Pld3* silencing is associated with increased A $\beta$  levels, and *PLD3*  
88 overexpression is associated with reduced A $\beta$  levels [4]. Thus, *PLD3* may play a broader role in  
89 LOAD.

90 Here, we sought to define the contribution of *PLD3* risk variants to AD-related  
91 phenotypes in human stem cell models and the role of *PLD3* in amyloid pathology in mouse

92 models. We found that a *PLD3* risk variant is sufficient to increase A $\beta$  levels in stem cell-derived  
93 neurons. In animal models of amyloid accumulation, *Pld3* silencing reduces A $\beta$  turnover and  
94 alters the composition of amyloid plaques. In the absence of *Pld3*, microglia recruitment to  
95 plaques is attenuated. Together, this study suggests that PLD3 contributes AD pathogenesis via  
96 A $\beta$  clearance through cell-autonomous and non-cell-autonomous pathways.

97

## 98 **Materials and Methods**

### 99 *Patient Consent*

100 Skin biopsies were collected following written informed consent from the donor. The  
101 Washington University School of Medicine Institutional Review Board and Ethics Committee  
102 approved the informed consent (IRB 201104178, 201306108). The consent allows for the use of  
103 tissue by all parties, commercial and academic, for research but not for human therapy.

104

### 105 *Dermal Fibroblast Isolation*

106 Dermal fibroblasts were isolated from skin biopsies obtained from the Knight Alzheimer  
107 Disease Research Center (ADRC) research participants. Briefly, skin biopsies were collected by  
108 surgical punch and stored in Fibroblast Growth Media (Lonza). To isolate dermal fibroblasts  
109 from a skin biopsy, the biopsies were rinsed with PBS and cut lengthwise with dissecting  
110 scissors. The resulting tissue sections were then plated into a dry 24-well tissue culture-treated  
111 plate (approximately 6-12 sections). After removing excess PBS from the wells, 300ul of  
112 fibroblast growth media (Lonza) was carefully added and tissue was incubated at 37°C and 5%  
113 CO<sub>2</sub>. After 24 hours, tissue was supplemented with 1mL fibroblast growth media and media  
114 changes were repeated every 3-4 days. Fibroblast cells migrated from the tissue within two  
115 weeks of culture. Dermal fibroblasts were maintained in fibroblast growth media (Lonza)  
116 supplemented with penicillin/streptomycin.

117

118 *iPSC Generation, Characterization, and Maintenance*

119 Human fibroblasts (F13504) were transduced with non-integrating Sendai virus carrying  
120 the four factors required for reprogramming: OCT3/4, SOX2, KLF4, and cMYC [11, 12]. Cells  
121 showing morphological evidence of reprogramming were selected by manual dissection.

122 Human iPSCs were cultured using feeder-free conditions (Matrigel, BD Biosciences,  
123 Franklin Lakes, NJ, USA). Human iPSCs were thawed ( $1-2 \times 10^6$  cells/mL), diluted in  
124 DMEM/F12, and centrifuged at 750 rpm for 3 minutes. The resulting iPSC pellet was then  
125 diluted in mTeSR1 supplemented with Rock inhibitor (Y-27632; 10 $\mu$ M final). iPSC were  
126 subsequently cultured in 37°C, 5% CO<sub>2</sub> with daily medium changes (mTeSR1, STEMCELL  
127 Technologies, Vancouver, BC, CA).

128 All iPSC lines were characterized using standard methods [11]. Each line was analyzed  
129 for pluripotency markers (OCT4A, SOX2, SSEA4, TRA1-80) by immunocytochemistry (ICC)  
130 (Invitrogen A24881) and quantitative PCR (qPCR); for chromosomal abnormalities by  
131 karyotyping; and for *PLD3* variant status by Sanger sequencing (Supplemental Figure 1).

132

133 *Genome editing*

134 We used CRISPR/Cas9 to generate isogenic control lines for the *PLD3* p.A442A iPSC  
135 as previously described [13]. The p3s-Cas9HC Cas9 expression plasmid (Addgene 43945) and  
136 CRISPR reagents (Addgene plasmid 43860) were used [14]. Guide RNAs were designed to  
137 overlap with the allele to be modified and have at least 3bp of mismatch to any other gene in the  
138 human genome. The activity of the guide was validated using a mismatch detection assay to  
139 determine non-homologous end-joining efficiency in K562 cells. A correctly edited clone and an  
140 unmodified clone were identified, expanded and characterized as described above for

141 karyotyping and pluripotency markers. Sanger sequencing was performed for the on-target and  
142 predicted off-target sites.

143

#### 144 *Cortical neuron differentiation*

145 IPSCs were differentiated into neuronal cells using a two-step approach as previously  
146 described [13]. IPSCs were plated at a density of 65,000 cells per well in neural induction media  
147 (STEMCELL Technologies) in a 96-well v-bottom plate to form highly uniform neural aggregates  
148 and, after five days, transferred onto culture plates. The resulting neural rosettes were then  
149 isolated by enzymatic selection (Neural Rosette Selection Reagent; STEMCELL Technologies)  
150 and cultured as neural progenitor cells (NPCs). NPCs were differentiated in planar culture in  
151 neuronal maturation medium (neurobasal medium supplemented with B27, GDNF, BDNF,  
152 cAMP). Neurons typically arise within one week after plating, identified using  
153 immunocytochemistry for  $\beta$ -tubulin III (Tuj1). The cells continued to mature and were analyzed  
154 at six weeks.

155

#### 156 *Immunocytochemistry*

157 IPSC-derived neurons were grown on PLO/laminin-coated 8-well chamber slides  
158 (Millipore). Culture media was aspirated, and cells were then washed and fixed with 4%  
159 paraformaldehyde (Sigma). After several washes, cells were permeabilized with 0.1% Triton X-  
160 100 in PBS. Cells were then blocked in 0.1% bovine serum albumin (BSA; Sigma) and treated  
161 with primary (Tuj1) and secondary antibodies diluted in 0.1% BSA. Immunostained cells were  
162 then imaged (Nikon Eclipse 80i fluorescent microscope).

163

#### 164 *Transcriptomics and Digital Deconvolution*

165 RNA was extracted from iPSC-derived neurons from *PLD3* p.A442A vs. the isogenic  
166 controls using Tissue Lyser LT and RNeasy Mini Kit (Qiagen, Hilden, Germany). RNA-seq

167 paired-end reads with read lengths of  $2 \times 150$  bp were generated using Illumina HiSeq 4000  
168 with a mean coverage of 80 million reads per sample. FastQC was applied to perform quality  
169 control and aligned to human GRCh37 primary assembly using Star (ver 2.5.2b). We applied  
170 Salmon transcript expression quantification (ver 0.7.2) to infer the gene expression. To estimate  
171 the relative proportion of major brain cell types in the dish, digital deconvolution was performed  
172 as previously described using a reference marker panel [15].

173

#### 174 *PLD3 Splicing Assay*

175 RNA was extracted from cell lysates with an RNeasy kit (Qiagen) according to the  
176 manufacturer's protocol. Extracted RNA (10ug) was converted to cDNA by PCR using the High-  
177 Capacity cDNA Reverse Transcriptase kit (ABI). SYBR-green primers were designed using  
178 Primer Express software, Version 3 (ABI). Real-time PCR assays were used to quantify *PLD3*  
179 exon 7 (forward primer: GCAGCTCCATCCCATCAACT; reverse:  
180 CTTGGTTGTAGCGGGTGTCA), exon 8 (forward primer: CTCAACGTGGTGGACAATGC;  
181 reverse: AGTGGCAGGTAGTTCATGACA), exon 9 (forward primer:  
182 ACGAGCGTGGCGTCAAG; reverse: CATGGATGGCTCCGAGTGT), exon 10 (forward primer:  
183 GGTCCCCGCGGATGA; reverse: GGTTGACACGGGCATATGG) and exon 11 (forward primer:  
184 GCTGCTGGTGACGCAGAAT; reverse: AGTCCCAGTCCCTCAGGAAAA). Each qPCR  
185 analysis included technical replicates and biological triplicates. Real-time data were analyzed  
186 using the comparative Ct method. Only samples with a standard error of <15% were analyzed.  
187 The Ct values for exon 11 were normalized with the Ct value for exons 7-10. The relative exon  
188 11 levels for the iPSC-derived neurons from *PLD3* p.A442A vs. the isogenic control were  
189 compared using a Tukey's t-test.

190

#### 191 *A $\beta$ Measurements*



192           Conditioned medium was collected from neurons after six weeks in culture and  
193 centrifuged at 3,000xg at 4°C for 10 minutes to remove cell debris. The levels of A $\beta$ 42 and  
194 A $\beta$ 40 were measured in cell culture media by sandwich ELISA as described by the  
195 manufacturer (Life Technologies). To account for variability in transfection efficiency between  
196 experiments, ELISA values were obtained (pg/mL) and corrected for total intracellular protein  
197 (ug/mL). Statistical difference was measured using an unpaired Student's t-test.

198

### 199 *PLD3 expression in AD and neuropathology free human brains*

200           Laser microdissected neurons from AD and control brains were previously reported and  
201 deposited as GSE5281 [38]. Brain samples were analyzed from 47 individuals of European  
202 descent clinically and neuropathologically confirmed AD cases or controls. The 33 AD samples  
203 were 54.5% female with a mean age of 79.9 years (range 73–86.8) and an average postmortem  
204 interval (PMI) of 2.5 hours. The 14 control brains were 28.6% female with a mean age of 79.8  
205 years (range 70.1–88.9). Samples were obtained from the entorhinal cortex, hippocampus,  
206 medial temporal gyrus, posterior cingulate, superior frontal gyrus, and primary visual cortex.  
207 RNA expression was measured using an Affymetrix GeneChip for gene expression. The log-  
208 transformed expression values were analyzed with brain region, age, and sex as covariates to  
209 analyze RNA expression.

210           Gene expression was analyzed in a second, independent, publicly available dataset of  
211 the temporal cortex of 76 control and 80 AD brains (syn6090813). Differential gene expression  
212 comparing controls v. AD was performed using a “Simple Model”, multi-variable linear  
213 regression analyses were conducted in R, using normalized gene expression measures  
214 including sex, age-at-death, RNA integrity number, brain tissue source, and flowcell as  
215 covariates [16]. Statistical difference was measured using an unpaired Student's t-test.

216

## 217 *Single nuclei RNAseq in human brains*

218 Human parietal cortices were processed to isolate nuclei, and the nuclei were then  
219 sequenced using the 10X Chromium single cell Reagent Kit v3, with 10,000 cells per sample  
220 and 50,000 reads per cell for each of the 74 samples as previously described [17, 18]. The  
221 Cell Ranger (v3.0.2 10XGenomics) software was used to align the sequences and quantify gene  
222 expression. We used the GRCh38 (3.0.0) reference to prepare a pre-mRNA reference. Filtering  
223 and QC were done using the Seurat package (3.0.1) on each subject individually. After the  
224 Uniform Manifold Approximation and Projection (UMAP) analysis was performed with the top 14  
225 PCs, we then used Seurat *FindNeighbors* and *FindClusters* functions to identify unique cell  
226 states or subclusters. Samples included in the subsequent analyses are summarized in  
227 Supplemental Table 1. To identify associations between cell-type transcriptional state and  
228 disease status or genetic strata (control, sporadic AD (sAD), TREM2), we applied linear  
229 regression models to test the cell state compositions of each subject. The proportions were  
230 normalized using a cube root transformation and were corrected by sex and age of death.  
231 Differentially expressed genes among the individual cell states were identified using a linear  
232 mixed model that corrected for sex and subject. To determine if there was unique functionality  
233 or potentially altered expression levels associated with disease/genetic carriers in the alternative  
234 cell states, we employed linear mixed model that predicted the expression level of each gene,  
235 modeled as zero-inflated negative binomial distributions and corrected for sex and age of death.  
236 Donors were modeled as random variables as previously described [17]. Data can be publicly  
237 accessed at <http://ngi.pub/SNARE>.

238

## 239 *Mouse Models*

240 Animal care and surgical procedures were approved by the Animal Studies Committee  
241 of Washington University School of Medicine in accordance with guidelines of the United States  
242 National Institutes of Health. APP<sup>swe</sup>/PS1 $\Delta$ E9 transgenic mice (APP/PS1; The Jackson

243 Laboratory; 034829) [19] of both sexes were used in this study. APP/PS1 mice were maintained  
244 on a C57bl6;C3B6 mixed background.

245 *Pld3*-KO mice were generated using CRISPR/Cas9 technology. gRNAs were designed  
246 to target an early conserved exon (mPld3.g19; TGCTGTGAGCACCGGCAAGGNGG). Guide  
247 activity was assessed in mouse neuroblastoma cells (N2A) using a T7E1 mismatch detection  
248 assay as previously described [13]. RNA was injected into the pronuclei of fertilized, viable  
249 murine oocytes isolated from a set of C57Bl/6xCBA (hybrid) female mice. Founders were  
250 identified using mPLD3 screening primers SM406.Cel.F 5' CATGGGCACTGTATCCCATCT 3'  
251 and SM406.Cel.R 5' AGGACACAAAAACGTCACCCT 3', which generated a parental band  
252 (575bp) and fragments (307 and 268bp). Subsequent generations were backcrossed to  
253 C57Bl/6;C3B6 (Supplemental Figure 2).

254 APP/PS1 mice were crossed with the *Pld3*-KO mice to generate APP/PS1x*Pld3*<sup>+/-</sup>.  
255 APP/PS1x*Pld3*<sup>+/-</sup> were crossed to obtain APP/PS1x*Pld3*-KO (APP/PS1x*Pld3*<sup>-/-</sup>) mice and  
256 APP/PS1x*Pld3*-WT (APP/PS1x*Pld3*<sup>+/+</sup>) littermates. Animals of both sexes were used in the  
257 study.

258

### 259 *Intracranial AAV-mediated expression of PLD3 and shPLD3*

260 Adeno-associated virus (AAV8) particles were generated that express AAV-CMV-  
261 hPLD3-WT-GFP, AAV-CMV-GFP (control), AAV-U6-shPLD3-GFP, and AAV-U6-shScrambled-  
262 GFP (control). Viral particles were injected into the hippocampus of APP/PS1 mice of both  
263 sexes to produce widespread transduction in hippocampal neurons as previously described [20,  
264 21]. Two  $\mu$ L of AAV particles ( $1.5 \times 10^{12}$  vg/ml) were stereotaxically injected bilateral  
265 hippocampi (2 $\mu$ l over 10 minutes) in 3-month-old APP/PS1 transgenic mice (prior to plaque  
266 appearance) [22, 23]. Virus is detectable at least 4-5 months post-injection [21, 24].

267

### 268 *In Vivo Microdialysis*

269 Prior to plaque accumulation (5 months of age) and two months post AAV8-injection,  
270 hippocampal ISF A $\beta$  levels were quantified using microdialysis in APP/PS1 mice as previously  
271 described [25, 26]. The use of a 38-kDa MWCO semi-permeable membrane allows for  
272 molecules smaller than this cut-off to diffuse into the probe. The probe was flushed with  
273 perfusion buffer at a constant rate (1.0 $\mu$ l/minute) and collected into a refrigerated fraction  
274 collector, and then assayed by sandwich ELISA (A $\beta_{x-40}$ ). A mouse monoclonal anti-A $\beta_{40}$  capture  
275 antibody (mHJ2) made in-house was used in conjunction with a biotinylated central domain  
276 detection antibody (mHJ5.1) and streptavidin-poly-HRP-40 (Fitzgerald Industries, Acton,  
277 MA)[27]. During microdialysis, mice were housed in cages that permit free movement and ad-  
278 libitum food/water, while ISF A $\beta$  was sampled. Baseline levels of ISF A $\beta$  were sampled every 60  
279 minutes between hours 5-12 (after the microdialysis probe insertion) and averaged to determine  
280 the baseline ISF A $\beta$  levels in each mouse. At hour 12, mice were administered the  $\gamma$ -secretase  
281 inhibitor Compound E (20mg/kg), intraperitoneally, which enabled us to determine the  
282 elimination half-life of ISF A $\beta$  [28]. A $\beta$  half-life was calculated using first-order kinetics.  
283 Microdialysis was performed with sham and littermate controls. Statistical difference was  
284 measured using an unpaired Student's t-test.

285 To evaluate the impact of *Pld3* on A $\beta$  kinetics, APP/PS1x*Pld3*-WT and APP/PS1x*Pld3*-  
286 KO mice were implanted at one-month post-injection with a microdialysis probe with a 38-kDa  
287 MWCO probe, and ISF was collected as described above. After 12 hours,  $\gamma$ -secretase inhibitor  
288 LY411575 (3mg/kg in 50:50PBS:PEG400) was administered intraperitoneally to define the  
289 elimination half-life of ISF A $\beta$ . A $\beta$  half-life was calculated as described above. Microdialysis was  
290 performed with sham and littermate controls. Statistical difference was measured using an  
291 unpaired Student's t-test.

292

293 *Brain Tissue Preparation*

294 APP/PS1x*Pld3*-WT and APP/PS1x*Pld3*-KO mice were anesthetized with sodium  
295 pentobarbital and perfused with 0.3% heparin in PBS at nine months of age. Brains were  
296 dissected and cut into two hemispheres. The right hemisphere was snap-frozen on dry ice and  
297 stored at 80°C for biochemical analyses. The left hemisphere was fixed in 4%  
298 paraformaldehyde for 24 hours, followed by 30% sucrose in PBS at 4°C. Coronal sections (50  
299 µm) were cut on a freezing-sliding microtome. Collected slices were stored in cryoprotectant  
300 solution (0.2 M phosphate-buffered saline, 30% sucrose, and 30% ethylene glycol) at -20°C.  
301

### 302 *Immunohistochemistry*

303 APP/PS1x*Pld3*-WT and APP/PS1x*Pld3*-KO brains were cut into 50µm sections from the  
304 rostral anterior commissure to the caudal hippocampus. Brains sections (n=20 mice per group)  
305 were incubated in 0.3% H<sub>2</sub>O<sub>2</sub> in Tris-buffered saline (TBS) for 10 minutes and blocked in 3%  
306 milk in TBS-X for 30 minutes. Tissue was incubated in HJ3.4B antibody (anti-Aβ-1-13; 2.4  
307 µg/ml; a generous gift from the Holtzman lab) overnight [29]. Sections are then incubated in  
308 Vectastain ABC elite solution in TBS (1:400) for 1 hour before incubating in 3,3'-  
309 Diaminobenzidine (DAB) solution. Sections were then mounted onto slides with Cytoseal  
310 (Thermo Scientific 8312-4). A Nanozoomer Digital Scanner (Hamamatsu Photonics) was used  
311 to create high-resolution digital images for the HJ3.4-stained brain slices. Total plaque  
312 coverage, total plaque count, and average plaque size were analyzed using NIH ImageJ  
313 software. Total plaque coverage was expressed as a percentage of the total area for each slice  
314 and averaged across the three slices per animal. Plaque count was expressed as the plaque  
315 count per nm<sup>2</sup> averaged across the three slices per animal. Plaque size was expressed in µm<sup>2</sup>  
316 averaged across all three slices for each mouse. Both the hippocampus and cortex were  
317 analyzed separately for each slice. Statistical difference for plaque size, percentage of total  
318 area, and plaque count per square millimeter was measured using an unpaired Student's t-test.  
319

320 *X-34 Plaque Staining*

321 To evaluate X-34 positive plaque burden, frozen coronal brain sections (50  $\mu\text{m}$ ) were  
322 mounted on Superfrost Plus slides, permeabilized with 0.25% Triton X-100 in PBS for 30  
323 minutes and stained with X-34 (0.01mM; Sigma SML1954) dissolved in 40% ethanol in PBS, pH  
324 10 for 20 min. The tissue was then washed with 40% ethanol in PBS and mounted with  
325 Fluoromount G mounting medium. Slides were imaged using Cytation7 (BioTek) and quantified  
326 using NIH ImageJ software. A Cytation7 cell imaging multi-modal imager was used to create  
327 high-resolution images of the X-34 scanned brain sections. Total plaque coverage, total plaque  
328 count, and average plaque size were analyzed using NIH ImageJ software. Total plaque  
329 coverage was expressed as a percentage of the total area for each section and averaged  
330 across three sections per animal. Plaque count was expressed as the plaque count per square  
331 millimeter averaged across the three sections per animal. Plaque size was expressed in square  
332 microns averaged across all three sections for each mouse. Both the hippocampus and cortex  
333 were analyzed separately for each section. Statistical difference for plaque size, percentage of  
334 total area, and plaque count per square millimeter was measured using an unpaired Student's t-  
335 test.

336

337 *Immunofluorescence*

338 Coronal brain sections (50 $\mu\text{m}$ ) were permeabilized in 0.25% Triton X-100 for 30 min at  
339 room temperature. Slices were then stained with X-34 (0.001 mM; Sigma SML1954) dissolved  
340 in 40% ethanol in PBS for 20 min and blocked in 3% BSA/3% Normal Donkey serum in 0.1%  
341 Triton X-100 in PBS. X-34-stained samples were immunostained with antibodies HJ3.4  
342 (2.4 $\mu\text{g}/\text{mL}$ ;  $\alpha\text{-A}\beta\text{1-13}$ ) or Iba1 (Abcam ab5076) and CD68 (BioRad MCA1957) at 4°C overnight.  
343 Three slices per animal were stained. Secondary antibodies of Alexa Fluor 488-conjugated  
344 donkey anti-rat IgG, Alexa Fluor 647-conjugated donkey anti-goat, and Alexa Fluor 647 donkey  
345 anti-mouse (Invitrogen). Slides were mounted with Fluoromount G mounting media. High

346 resolution 40x images were obtained using the Zeiss LSM 880 Confocal microscope with  
347 Airyscan. Z-stacks were analyzed using NIH ImageJ software, where max projection images  
348 (those with the highest signal intensity) were selected for each fluorescent channel. The Iba1  
349 and CD68 signals were quantified within 15 $\mu$ m of the X-34-positive plaques. Iba1 and CD68  
350 colocalization was also quantified. An outlier analysis was run using the ROUT method with a  
351 Q-value of 1%. Three outliers were removed from the APP/PS1x*Pld3*-KO mice in the Iba1  
352 analysis. Statistical difference was measured using an unpaired Student's t-test.

353 To quantify HJ3.4 and X-34 colocalization, Z-stacks were analyzed using NIH ImageJ  
354 software, where max projection images were selected for each fluorescent channel. Plaque  
355 composition was quantified by measuring the percentage of HJ3.4 staining within X-34-positive  
356 areas. Nonfibrillar plaque area was normalized to the total X-34 area. A ROUT outlier analysis  
357 with a Q-value of 1% was run for each of these quantifications. No outliers were removed from  
358 the analysis of percent area. Four outliers were excluded in the APP/PS1x*Pld3*-WT mice, and  
359 three outliers were excluded in the APP/PS1x*Pld3*-KO mice in the nonfibrillar plaque area  
360 analysis. Statistical difference was measured using an unpaired Student's t-test.

361

## 362 **Results**

363 *AD risk variant PLD3 p.A442A is sufficient to alter PLD3 splicing and A $\beta$  levels*

364 Three highly conserved, rare variants in *PLD3* increase AD risk: p.M6R, p.V232M, and  
365 p.A442A [4]. *PLD3* p.A442A (G>A) was associated with increased AD risk in four independent  
366 case-control datasets ( $p=3.78\times 10^{-7}$ ; OR=2.12) [4]. *PLD3* p.A442A was predicted to modify a  
367 splicing enhancer-binding site, SRSF1, *in silico* [4]. In the brains of *PLD3* p.A442A carriers, total  
368 *PLD3* and exon 11-containing transcript expression were reduced compared to controls [4].  
369 However, these association studies did not allow us to attribute the causality of the risk variant  
370 to the phenotype.

371 Here, we coupled genome-editing with stem cell models to determine whether *PLD3*  
372 p.A442A is sufficient to alter *PLD3* splicing and phenocopy AD-related phenotypes. Primary  
373 dermal fibroblasts were obtained from a patient carrying a single copy of the *PLD3* p.A442A  
374 variant. Fibroblasts were de-differentiated into induced pluripotent stem cells using non-  
375 integrating Sendai virus. The resulting iPSC were characterized for pluripotency markers, the  
376 presence of the *PLD3* p.A442A variant, and chromosomal integrity (Supplemental Figure 1). To  
377 determine the causality of *PLD3* p.A442A on AD-related phenotypes, we used CRISPR/Cas9 to  
378 correct the A allele to G (wild-type) (Figure 1A) [13]. *PLD3* p.A442A and isogenic controls (*PLD3*  
379 WT) were then differentiated into cortical neurons using a growth factor-mediated approach as  
380 previously described (Figure 1A) [13], where they illustrated a similar capacity to form Tuj1-  
381 positive neurons (Figure 1B). To further verify the similarity between the cells in their capacity to  
382 form neurons, we estimated the relative proportion of neurons in the cultures using bulk  
383 transcriptomics and deconvolution methods that include all the major brain cell types [15]. We  
384 found that differentiated cultures from *PLD3* p.A442A and isogenic controls exhibited a similar  
385 enrichment of neurons (~95%; Figure 1C). These findings are consistent with a variant that  
386 impacts a late-onset disease, where we would not predict a significant developmental defect.

387 Having demonstrated that *PLD3* p.A442A and isogenic controls share a similar capacity  
388 to form neurons, we next asked whether the *PLD3* p.A442A variant was sufficient to alter *PLD3*  
389 splicing in a manner consistent with our prior observations in human brains from *PLD3* p.A442A  
390 carriers [4]. RNA isolated from neurons expressing *PLD3* p.A442A and isogenic controls was  
391 converted to cDNA, and *PLD3* exons 7, 8, 9, 10, and 11 were amplified and quantified. We  
392 found that *PLD3* exons are significantly reduced in the *PLD3* p.A442A neurons, which is  
393 restored upon correction of the variant allele to WT (Figure 1D). To determine whether *PLD3*  
394 p.A442A neurons exhibit changes in A $\beta$ , which would be consistent with a variant that impacts  
395 amyloid plaque deposition, we measured extracellular A $\beta$  by sandwich ELISA in the media of  
396 *PLD3* p.A442A and isogenic control neurons. After correcting for total protein, we observed a



397 significant increase in A $\beta$ 42 and A $\beta$ 40 in media from neurons expressing *PLD3* p.A442A (Figure  
398 1E and 1F) without changing the A $\beta$ 42/40 ratio (Figure 1G) when compared to isogenic controls.  
399 Together, these findings illustrate that in nearly identical, isogenic neurons, the presence of the  
400 *PLD3* p.A442A is sufficient to alter *PLD3* transcripts and extracellular A $\beta$  levels.

401

#### 402 *PLD3* expression is altered in LOAD brains

403 Having demonstrated that the AD risk variant in *PLD3* (*PLD3* p.A442A) was sufficient to  
404 alter *PLD3* transcripts and A $\beta$  levels, we sought to determine whether *PLD3* is altered in LOAD.  
405 We examined *PLD3* expression in laser-captured microdissected neurons across multiple brain  
406 regions from AD cases and neuropathology-free controls. *PLD3* expression was significantly  
407 lower in AD brains compared with control brains in the entorhinal cortex, hippocampus, medial  
408 temporal gyrus, and superior frontal gyrus (Figure 2), regions that exhibit amyloid and tau  
409 pathology. Interestingly, *PLD3* expression was unaltered in the primary visual cortex, which is  
410 largely spared of AD pathology (Figure 2) [30]. *PLD3* expression was also significantly reduced  
411 in an independent cohort of temporal cortices isolated from AD and control brains ( $\beta=-0.36$ ;  
412  $p=3.23\times 10^{-4}$ ) [16]. These findings are consistent with prior reports of reduced *PLD3* expression  
413 in LOAD brains [4].

414

#### 415 *Pld3* regulates A $\beta$ in APP/PS1 mice

416 *PLD3* expression is reduced in brains from *PLD3* p.A442A carriers and in LOAD brains  
417 (Figure 2) [4], and overexpression or silencing of *PLD3* in mouse neuroblastoma cells leads to  
418 inverse changes in A $\beta$  levels [4]. Thus, we sought to determine whether modulating *PLD3*  
419 expression is sufficient to alter A $\beta$  *in vivo*. In mice, A $\beta$  is primarily generated in neurons and  
420 released into the ISF, where it can be cleared by extracellular proteolysis, transported into CSF  
421 or across the blood-brain barrier, or by cellular uptake and degradation. The steady-state level  
422 of ISF A $\beta$ , thus, reflects these production and degradation/clearance mechanisms. We

423 hypothesized that reducing endogenous *Pld3* expression, as observed in human AD brains,  
424 would elevate ISF A $\beta$  levels. To address this hypothesis, 3-month-old APP/PS1 mice were  
425 injected with AAV8 particles containing sh*Pld3* or shScrambled (control) and evaluated at five  
426 months of age by *in vivo* microdialysis (Figure 3A). At five months of age, sh*Pld3* was sufficient  
427 to significantly reduce endogenous *Pld3* transcript level in the hippocampus compared with  
428 scrambled controls by 28% (Figure 3B). This modest reduction of *Pld3* did not alter steady-state  
429 ISF A $\beta$  levels (Figure 3C and 3D;  $p=0.27$ ). Next, to test the impact of *Pld3* silencing on the A $\beta$   
430 elimination rate (half-life), A $\beta$  levels were monitored after treatment with a  $\gamma$ -secretase inhibitor  
431 (Figure 3C). The secretase inhibitor rapidly blocks A $\beta$  generation within minutes, then ISF is  
432 sampled hourly to calculate the rate of elimination of existing A $\beta$ . Silencing of *Pld3* resulted in a  
433 135% increase in A $\beta$  elimination half-life (Figure 3C and 3E;  $p=0.0025$ ). Thus, PLD3 is likely  
434 involved in A $\beta$  clearance.

435 The striking impact of a modest *Pld3* decrease in A $\beta$  levels in the APP/PS1 mice led us  
436 to investigate the impact of a global knockout of *Pld3* on A $\beta$  (Figure 3F). Global *Pld3* knockout  
437 mice were generated using CRISPR/Cas9. A guideRNA targeting an early, highly conserved  
438 exon was validated *in vitro* and injected into murine oocytes (see Methods; Supplemental Figure  
439 2). Founders were established and backcrossed to C57Bl/6;C3B6 prior to breeding with  
440 APP/PS1 mice (Supplemental Figure 3C). Consistent with prior reports, *Pld3* KO mice were  
441 viable and did not exhibit gross defects [9, 31]. *Pld3*-deficient APP/PS1 mice exhibited a 35%  
442 increase in steady-state ISF A $\beta$  at four months of age (Figure 3G-3I). In agreement with the  
443 AAV-mediated knockdown, *Pld3*-deficient APP/PS1 mice exhibited a 49% increase in A $\beta$   
444 elimination half-life following the administration of a  $\gamma$ -secretase inhibitor (Figure 3G and 3I).  
445 Thus, *Pld3* reduction in the brain is sufficient to reduce the turnover of ISF A $\beta$ .

446 *In vitro* overexpression of PLD3 was sufficient to reduce extracellular A $\beta$  [4]. Thus, we  
447 asked whether overexpression of *hPLD3* in APP/PS1 mice could rescue the ISF A $\beta$  phenotype  
448 (Figure 3A). The hippocampus of APP/PS1 mice was bilaterally injected with AAV8 particles

449 containing hPLD3 or GFP (control) at three months of age, and two months later, ISF A $\beta$  was  
450 measured by microdialysis (Figure 3A). Overexpression of *hPLD3* significantly reduced steady-  
451 state levels of ISF A $\beta$  and A $\beta$  elimination half-life by approximately 25% (Figure 3J-M). Taken  
452 together, our findings illustrate that PLD3 expression regulates A $\beta$  turnover in APP/PS1 mice.

453

#### 454 *Pld3-deficiency alters plaque composition*

455 Impairment in protein clearance has been implicated in amyloid plaque accumulation  
456 and AD pathogenesis [32, 33]. A $\beta$  aggregation in the extracellular space (ISF) into soluble  
457 oligomers or insoluble amyloid plaques is a critical driver of AD pathogenesis, and conversion of  
458 monomeric A $\beta$  into these aggregates is facilitated at higher concentrations [34]. Thus, we  
459 sought to determine whether increased ISF A $\beta$  in four months old APP/PS1x*Pld3*-KO mice  
460 could impact amyloid plaque pathology in older animals (Figure 4A). To assess plaque  
461 pathology, APP/PS1x*Pld3*-KO mice were sacrificed at nine months of age, and brain sections  
462 were co-stained with HJ3.4 (total A $\beta$ ) and X-34 ( $\beta$ -sheet rich dense cores; Figure 4B). Plaque  
463 composition was then analyzed as the percent of X-34 stain within HJ3.4-positive plaques  
464 (termed: fibrillar plaques) and the extent of HJ3.4-positivity outside X-34 plaques (termed: Non-  
465 fibrillar plaque area). In APP/PS1x*Pld3*-KO mice, the percentage of fibrillar plaques was  
466 significantly reduced compared with APP/PS1x*Pld3*-WT mice (Figure 4C). Conversely, the non-  
467 fibrillar plaque area was significantly increased compared with APP/PS1x*Pld3*-WT mice (Figure  
468 4D). In complementary analyses, we found that A $\beta$  plaque size was significantly increased in  
469 the cortex of APP/PS1x*Pld3*-KO compared with APP/PS1x*Pld3*-WT mice (Supplemental Figure  
470 3) without a change in the overall plaque burden as defined by the percentage area of HJ3.4-  
471 positive immunostaining (e.g., plaque density). X-34 staining remained unchanged in the  
472 absence of *Pld3* (Supplemental Figure 4). Thus, *Pld3* KO impacts plaque composition, shifting  
473 the pathology to a less fibrillar structure [35].

474

475 *Pld3* deficiency impact microglial recruitment to amyloid plaques

476           The absence of *Pld3* in the APP/PS1 mice resulted in more non-fibrillar plaques. This  
477 shift in plaque composition is similar with findings from *Trem2*- and *ApoE*-deficient APP/PS1  
478 mice [36-39]. Loss of these AD risk genes also significantly reduced microglial recruitment to the  
479 amyloid plaques [36-39]. Thus, we hypothesized that the loss of *Pld3* may alter the microglial  
480 response in APP/PS1 mice. To test this hypothesis, fixed brain tissue from the APP/PS1x*Pld3*-  
481 KO and APP/PS1x*Pld3*-WT mice were stained for total microglia (Iba1), activated microglia  
482 (CD68), and dense core A $\beta$  plaques (X-34) (Figure 5A). The amount of activated microglia as a  
483 percentage of total microglia was similar between APP/PS1x*Pld3*-KO and APP/PS1x*Pld3*-WT  
484 mice (Figure 5D). However, APP/PS1x*Pld3*-KO mice exhibited a significant reduction in the  
485 recruitment of microglia around the X-34-positive plaques (Figure 5B). No significant change  
486 was observed in the amount of CD68-positive, activated microglia around the X-34-positive  
487 (Figure 5C and 5D). *Pld3* deficient APP/PS1 mice also exhibited a significant increase in  
488 expression of microglia genes associated with neurodegeneration including *Trem2*, *Tyrobp*,  
489 *Ctsd*, and *Cst7* (Table 1) without a corresponding change in homeostatic microglia genes (Table  
490 1). Thus, loss of *Pld3* impacts microglia function in response to amyloid plaques.

491

492 *A role for PLD3 in microglia*

493           Given the association of *Pld3* loss with altered microglia function in mouse models, we  
494 sought to determine whether *PLD3* is altered in microglia in human brains. Nuclei were isolated  
495 and sequenced from frozen AD and age-matched control brains (Figure 6A)[17, 18]. AD brains  
496 were further classified based on the presence of *TREM2* risk variants (named: TREM2).  
497 Unsupervised clustering of the brain nuclei revealed 15 cell-type specific clusters that  
498 correspond to the major cell-types found in the brain [17]. We isolated microglia from other cells  
499 and reexamined the alternative transcriptional states that we further classified into nine

500 subclusters (Figure 6B). *PLD3* expression was significantly overexpressed in Mic.1 and reduced  
501 Mic.2 microglia subclusters compared to all microglia clusters (Figure 6B;  $p=2.71\times 10^{-5}$  and  
502  $2.27\times 10^{-6}$ , respectively; Supplemental Table 2). In contrast, homeostatic microglia (Mic.0) did  
503 not show differential expression of *PLD3* (Figure 6B;  $p=0.52$ ; Supplemental Table 2). Microglia  
504 in Mic.1 have an expression signature consistent with microglia associated with  
505 neurodegeneration (e.g. disease associated or activated response microglia) [40-42], while  
506 Mic.2 clusters are enriched among *TREM2* variant carriers and exhibit upregulated resting state  
507 microglia markers with minimal elevation of genes associated with activated microglia [17].

508 To understand how *PLD3* expression changes in microglia with disease, we examined  
509 control, sporadic AD and *TREM2* risk variant carriers. *PLD3* expression was significantly  
510 reduced in homeostatic microglia in sporadic AD brains and *TREM2* risk variants compared to  
511 controls (Figure 6C;  $p=1.04\times 10^{-3}$  and  $p=2.46\times 10^{-2}$ , respectively; Supplemental Table 3). *PLD3*  
512 expression was further dysregulated in disease associated Mic.1 cluster in *TREM2* risk variant  
513 carriers compared with controls (Figure 6D;  $p=4.13\times 10^{-3}$ ; Supplemental Table 3).

514 To further clarify the relationship between *PLD3* and microglia function, we analyzed  
515 *PLD3* expression in single cell RNAseq data obtained from human iPSC expressing inducible  
516 CRISPRi machinery that were transduced with 81 sgRNAs and differentiated into iTF-Microglia  
517 (Figure 6E) [43]. Unsupervised clustering analyses revealed nine distinct microglia subclusters  
518 (Figure 6E), representing distinct transcriptional states. Among these subclusters, *PLD3* was  
519 significantly overexpressed in clusters 1, 2, and 3 and significantly reduced in clusters 4, 5, 7,  
520 and 9 (Figure 6F and 6G; Supplemental Table 4). Clusters 1-3 correspond with interferon-  
521 induced gene activation states [43], while clusters 4-9 are enriched for genes associated with  
522 chemokine/cytokine activation states [43]. Cluster 3, where *PLD3* is significantly elevated, is  
523 enriched in *SPP1* expression, a marker of disease associated microglia [43]. Additionally,

524 cluster 7, where *PLD3* is significantly reduced, is enriched in markers of microglia proliferation  
525 [43]. Together, these data support a role for *PLD3* in microglia activation in health and disease.

526

## 527 **Discussion**

528 In this study, we sought to understand the contribution of *PLD3* to pathways that  
529 promote AD pathology. We demonstrate that the AD risk variant, *PLD3* p.A442A, is sufficient to  
530 alter *PLD3* splicing and A $\beta$  levels in iPSC-derived neurons in a manner consistent with similar  
531 findings in AD brains [4]. Additionally, we describe a role for *PLD3* in LOAD, whereby modifying  
532 *PLD3* expression in *APP/PS1* mice is sufficient to regulate A $\beta$  turnover in the ISF. The observed  
533 reduced ISF A $\beta$  turnover, in turn, leads to a change in amyloid plaques in aged animals. We  
534 observed that loss of *Pld3* in *APP/PS1* mice results in a shift in plaque composition to a more  
535 nonfibrillar structure. This altered plaque composition is accompanied by impaired microglial  
536 recruitment to the plaques, consistent with prior reports from *Trem2* deficient mice. In human  
537 brains, *PLD3* is enriched in disease associated microglia and expression is altered in AD brains.  
538 Together, these results suggest that *PLD3* plays cell-autonomous and non-cell autonomous  
539 roles in AD pathogenesis.

540 Deciphering the contribution of risk variants and pathogenic mutations to AD  
541 pathogenesis has led to groundbreaking discoveries of A $\beta$  metabolism, synaptic function, and  
542 immune function to AD and revealed novel therapeutic targets [44]. Emerging sequencing  
543 technologies in increasingly larger cohorts have revealed the contribution of rare variants to AD  
544 risk [44, 45]. Nevertheless, resolving the contribution of rare variants to disease can be  
545 challenging when relying on association studies and autopsy brain tissue that captures a  
546 snapshot of disease.

547 Here, patient-derived cell culture models represent a tractable, human platform that  
548 recapitulates disease-specific phenotypes and when coupled with genome engineering, allows

549 for the study of genotype x phenotype relationships. This study demonstrates that iPSC-derived  
550 neurons are highly informative and recapitulate early pathogenic events in AD.

551 In this study, we used genome editing technology to molecularly pinpoint the contribution  
552 of the A allele to PLD3 and AD-related phenotypes. While we cannot exclude the possibility that  
553 genomic factors beyond PLD3 p.A442A contribute to the risk profile in the iPSC donor line used  
554 in this study, we can attribute the defect in PLD3 splicing and the increase in A $\beta$  levels to this  
555 synonymous variant. The increase in both A $\beta$ 42 and A $\beta$ 40 is consistent with the effects of other  
556 known pathogenic mutations, including APP KM670/671NL [46, 47]. The absence of an effect of  
557 *PLD3* p.A442A on the A $\beta$ 42/40 ratio suggests that A $\beta$  recycling and trafficking. This is  
558 consistent with recently reported functions of PLD3 as a type II membrane protein functioning in  
559 endosomes and lysosomes, the primary site of APP cleavage [48, 49]. Together, these human  
560 stem cell findings suggest a role for PLD3 p.A442A in altering APP/A $\beta$  recycling and trafficking  
561 in a manner that elevates total A $\beta$  levels.

562 *PLD3* p.A442A was predicted to disrupt a splicing enhancer-binding site [4]. We observe  
563 defective *PLD3* splicing in iPSC-derived neurons from a *PLD3* p.A442A carrier, which replicates  
564 the observations in brains from *PLD3* p.A442A carriers [4]. We go on to demonstrate that  
565 correcting the risk allele with CRISPR/Cas9 is sufficient to restore the splicing defect. The  
566 functional impact of distinct PLD3 isoforms remains unknown; however, as the functional roles  
567 of PLD3 are resolved, this will be an important area to explore.

568 We show that PLD3 is a major regulator of ISF A $\beta$  turnover *in vivo*. Hippocampal  
569 reduction of endogenous *Pld3* in adulthood via AAV8-mediated knockdown or global knockout  
570 of *Pld3* in the background of APP/PS1 mice resulted in a strong increase in ISF A $\beta$  half-life,  
571 suggesting that A $\beta$  is turned over more slowly in the absence of *Pld3*. A $\beta$  clearance  
572 mechanisms have been proposed to drive LOAD [33]. Following secretion from presynaptic  
573 neurons, A $\beta$  is either taken up and degraded in the lysosomes of post-synaptic neurons, taken

574 up and degraded in the lysosomes of glial cells, degraded by extracellular proteases, is  
575 transported to CSF, or transcytosed across the blood-brain barrier (BBB). Amyloid accumulation  
576 occurs in an A $\beta$  concentration-dependent manner [34]; thus, dysregulation of ISF A $\beta$  clearance  
577 drives amyloid accumulation and AD pathogenesis. Neurons from *Pld3* KO mice exhibit  
578 lysosomes with increased density and size [31]. PLD3 is enriched in lysosomes surrounding  
579 amyloid plaques in human AD brains and mouse models of amyloid accumulation [9]. Thus,  
580 *Pld3* may regulate ISF A $\beta$  through lysosome-mediated clearance mechanisms in neurons or  
581 other glial cells.

582         The absence of *Pld3* in APP/PS1 mice led to a shift in the composition of amyloid  
583 plaques to being more diffuse and less fibrillar. While amyloid plaques may adopt a series of  
584 morphologies and architecture, a major structure is characterized by a dense “fibrillar” core of  
585 A $\beta$  surrounded by more diffuse “non-fibrillar” of A $\beta$  deposits [50]. Non-fibrillar A $\beta$  is proposed to  
586 contribute to its higher toxicity, possible because either its structure is more toxic or they serve  
587 as a reservoir for more diffusible A $\beta$  oligomers [35, 51]. Thus, a PLD3-mediated shift to more  
588 non-fibrillar plaques is consistent with more toxic effects given the same amount of overall A $\beta$   
589 deposition. Silencing AD risk genes, including *Trem2* and *ApoE*, result in a similar shift of  
590 plaque composition shift in APP/PS1 mice [36, 37, 39]. Thus, modeling the reduction of *PLD3*  
591 observed in *PLD3* p.A442A carriers, and LOAD brains in an animal model of amyloid  
592 accumulation leads to a phenotype consistent with a gene that exacerbates disease.

593         In prior studies where gene silencing in amyloid mice led to a change in plaque  
594 formation and composition, a role for an altered microglial response to amyloid plaques was  
595 implicated [36, 37, 39]. APP/PS1x*Pld3*-KO and APP/PS1x*Pld3*-WT mice exhibited a similar  
596 abundance of Iba1 positive microglia. Yet, recruitment of Iba1-positive microglia to X-34-positive  
597 plaques was significantly reduced in APP/PS1x*Pld3*-KO mice compared to APP/PS1x*Pld3*-WT  
598 mice. This could suggest a role for PLD3 in recruiting microglia to surround and alter A $\beta$



599 structure and limit A $\beta$ -induced toxicity similar to mechanisms described for TREM2 [36]. In mice,  
600 *Pld3* mRNA is expressed in microglia [52]. Microglia isolated from amyloid mouse models  
601 (APP<sup>NL-F-G</sup>) reveal an activation state enriched for MHC class II, tissue repair genes, and  
602 enrichment of AD risk genes, including *Pld3* [42]. Thus, loss of *Pld3* in the global knockout may  
603 impact the molecular identity of microglia, which impairs the recruitment and responsiveness of  
604 the glia to plaques.

605 In human microglia, PLD3 plays a role in microglia that is disrupted in AD. Microglia  
606 maintain distinct transcriptional states that likely reflect functional changes due to environmental  
607 stimuli [53]. We demonstrate that *PLD3* expression is enriched in disease associated microglia  
608 (Brain Mic.1 and iTF-Microglia cluster 3) and depleted in population of microglia that are found  
609 in *TREM2* risk variant carriers (Brain Mic.2). Mic.2 reflect a dampened activation state, distinct  
610 from homeostatic microglia (Mic.0) with an upregulation of resting state microglia markers  
611 (*TMEM119*, *P2RY13*, *MED12L*) and modest elevation of activated markers (*ABCA1*, *C5AR1*,  
612 and *CD83*) [17]. This finding along with the observation that *PLD3* expression is reduced in  
613 disease associated microglia (Mic.1) in *TREM2* risk variant carriers suggests a potential  
614 interaction between these AD risk genes. These results also support the parallels between our  
615 mouse model findings and those in *Trem2* deficient mice. In addition to association with disease  
616 associated microglia, PLD3 and TREM2 have also been implicated in lysosomal function [9, 31,  
617 38, 48, 49].

618 Overall, we observed a modest impact on amyloid plaque pathology in APP/PS1x*Pld3*-  
619 KO mice. The modest impact is highly consistent with PLD3 as a disease modifier rather than a  
620 fully penetrant, causative mutation. Alternatively, this could reflect redundant mechanisms for  
621 mouse *Pld3*.

622 Here, we demonstrate a therapeutic potential for *PLD3*. *hPLD3* overexpression by AAV8  
623 in APP/PS1 mice resulted in a significant decrease in ISF A $\beta$  levels and accelerated A $\beta$   
624 turnover. *PLD3* levels are significantly reduced in AD brains, and *PLD3* expression is positively  
625 correlated with cognition in humans and mouse models [9]. Thus, by promoting A $\beta$  turnover  
626 and facilitating the microglial response to amyloid plaques, *PLD3* occupies a crucial role in brain  
627 health.

628

## 629 **Disclosures**

630 D.M.H. co-founded and is on the scientific advisory board of C2N Diagnostics. D.M.H. is on the  
631 scientific advisory board of Denali and Cajal Neuroscience and consults for Genentech and  
632 Alector. CC has received research support from: Biogen, Eisai, Alector and Parabon. The  
633 funders of the study had no role in the collection, analysis, or interpretation of data; in the writing  
634 of the report; or in the decision to submit the paper for publication. CC is a member of the  
635 advisory board of Vivid genetics, Halia Therapeutics and ADx Healthcare. AMG is on the  
636 scientific advisory boards of Genentech and Muna Therapeutics. M. K. has filed a patent  
637 application related to CRISPRi and CRISPRa screening (PCT/US15/40449) and serves on the  
638 Scientific Advisory Board of Engine Biosciences, Casma Therapeutics, and Cajal Neuroscience,  
639 and is an advisor to Modulo Bio and Recursion Therapeutics. The remaining authors have no  
640 disclosures.

641

## 642 **Acknowledgments**

643 This work was funded by BrightFocus Foundation (CMK), the Alzheimer's Association  
644 (CMK), NIH U01 AG052411 (AG), R01 AG062359 (CMK), P50 AG005681 (JM, CMK),  
645 R56AG067764 (CMK, OH, CC), U01 AG072464 (ST, CMK, OH, MK), UL1 TR002345,  
646 NS090934 (DMH), AG047644 (DMH), NS094692 (JML), AG062359 (MK). This work was

647 supported by access to equipment made possible by the Hope Center for Neurological  
648 Disorders and the Departments of Neurology and Psychiatry at Washington University School of  
649 Medicine. We thank the Washington University in St Louis Mouse Genetics Core for assistance  
650 in generating the Pld3 KO mice. The gRNAs were generated by the Genome Engineering and  
651 iPSC Center (GEiC) at the Washington University in St. Louis. We thank the Hope Center Viral  
652 Vector Core for generating the AAV8 particles and the Hope Center Animal Surgery Core for  
653 performing the AAV8 injections. Confocal was generated on a Zeiss LSM 880 Airyscan  
654 Confocal Microscope, which was purchased with support from the Office of Research  
655 Infrastructure Programs (ORIP), a part of the NIH Office of the Director under grant OD021629.  
656 The recruitment and clinical characterization of research participants at Washington University  
657 were supported by NIH P50 AG05681, P01 AG03991, and P01 AG026276.

658

659

660 Table 1: Differential microglia gene expression in APP/PS1x*Pld3*-KO compared with  
661 APP/PS1x*Pld3*-WT brains

Gene	Log2FoldChange	p-value
<i>Trem2</i>	0.48	1.07E-03
<i>Tyrobp</i>	0.57	1.06E-03
<i>Ctsd</i>	0.25	4.18E-03
<i>Cst7</i>	0.56	2.91E-02
<i>Cd68</i>	0.35	6.27E-02
<i>Aif1</i>	0.33	1.08E-01
<i>Tmem119</i>	0.04	6.49E-01
<i>P2ry12</i>	0.05	5.99E-01

662

663 **Figure Legends**

664 **Figure 1: iPSC-neurons expressing *PLD3* p.A442A phenocopy splicing defects observed**

665 **in human brains** A. Fibroblasts from a *PLD3* p.A442A variant carrier were reprogrammed into  
666 induced pluripotent stem cells (iPSCs). CRISPR-Cas9 technology was used to generate an  
667 isogenic control line. iPSCs were then differentiated into cortical neurons (see Methods).  
668 Downstream assays were performed after 42 days in culture. B. iPSC-derived neurons stained  
669 with Tuj1 illustrate a similar capacity of p.A442A and isogenic controls (*PLD3* WT) to form  
670 neurons. C. Digital deconvolution of iPSC-derived neurons from transcriptomic data illustrates a  
671 similar enrichment of neurons in *PLD3* p.A442A and isogenic controls (*PLD3* WT). D.  
672 Expression of *PLD3* exon 11 compared to *PLD3* exons 7, 8, 9, and 10. E-G. Sandwich ELISA of  
673 media from iPSC-derived neurons (pg/mL) and corrected for total protein measured by BCA  
674 (pg/ $\mu$ g). A $\beta$ 42 (E), A $\beta$ 40 (F), A $\beta$ 42/40 (G). Graphs represent mean  $\pm$  SEM. \* $<0.05$ ,  
675 \*\*\*\* $<0.00005$ . Analyzed by two-tailed Student's *t* test.

676

677 **Figure 2: *PLD3* expression is significantly reduced in brain regions vulnerable to AD**

678 **pathology.** Laser capture of microdissected neurons from the brains of neuropathology  
679 confirmed control and AD brains [54]. Quantification of *PLD3* expression in laser microdissected  
680 neurons isolated from AD and control brains. The graph represents mean  $\pm$  SEM. \* $p<0.05$ .  
681 Analyzed by two-tailed Student's *t* test.

682

683 **Figure 3: Bi-directional expression of *Pld3* alters A $\beta$  turnover *in vivo*.** A-E. The impact of

684 *Pld3* silencing on ISF A $\beta$ . A. Diagram of the experimental timeline: APP/PS1 mice were injected  
685 with shScramble sh*Pld3* (compared to *shScram* control)-containing AAV8 particles at three

686 months of age and were evaluated by *in vivo* microdialysis at five months of age. *shScramble*  
687 (n=7) and *shPld3* (n=6). B. Knockdown of endogenous *Pld3*. C. A $\beta$  levels in ISF sampled over  
688 14 hours in *shScram*, and *shPld3* injected APP/PS1 mice. D. Steady-state levels of ISF A $\beta$ . E.  
689 Elimination half-life of ISF A $\beta$ . F-I. The impact of *Pld3* KO on ISF A $\beta$ . F. Diagram outlining the  
690 experimental timeline: APP/PS1x*Pld3*-WT and APP/PS1x*Pld3*-KO mice were evaluated by *in*  
691 *in vivo* microdialysis at four months of age. APP/PS1x*Pld3*-WT (n=10), APP/PS1x*Pld3*-KO (n=14).  
692 G. A $\beta$  levels in ISF sampled over 14 hours in APP/PS1x*Pld3*-WT and APP/PS1x*Pld3*-KO mice.  
693 H. Steady-state levels of ISF A $\beta$ . I. Elimination half-life of ISF A $\beta$ . J-M. APP/PS1 mice were  
694 injected with hPLD3 (compared to GFP control)-containing AAV8 particles at three months of  
695 age and were evaluated by *in vivo* microdialysis at five months of age. GFP (n=7), hPLD3 (n=8).  
696 J. Overexpression of *hPLD3*. K. A $\beta$  levels in ISF sampled over 14 hours in *GFP* and *hPLD3*  
697 injected APP/PS1 mice. L. Steady-state levels of ISF A $\beta$ . M. Elimination half-life of ISF A $\beta$ .  
698 Graphs represent mean  $\pm$  SEM. \* $<0.05$ , \*\*\* $<0.0005$ . Analyzed by two-tailed Student's *t* test.

699

700 **Figure 4: Loss of *Pld3* alters plaque composition in APP/PS1 mouse cortex.** A.

701 Experimental timeline. APP/PS1x*Pld3*-WT (n=20), APP/PS1x*Pld3*-KO (n=15). B.

702 Representative confocal images of mouse cortex co-stained with HJ3.4 (total A $\beta$ ) and X-34 ( $\beta$ -

703 sheet rich dense cores). C-D. Quantification of the plaque composition. C. Percent of X-34

704 within a HJ3.4-positive area. D. Area HJ3.4 outside of X-34-positive area (nonfibrillar area). The

705 total area of X-34 normalized signal microns. Graphs represent mean  $\pm$  SEM. \*\*,  $p=0.0010$ ; \*\*\*,

706  $p=0.0003$ . Analyzed by two-tailed Student's *t* test with a ROUT outlier analysis (Q=1%).

707

708 **Figure 5: Loss of *Pld3* alters the microglial response to A $\beta$  pathology.** A. Representative

709 images of APP/PS1x*Pld3*-WT and APP/PS1x*Pld3*-KO mice co-stained with Iba1 (total

710 microglia), CD68 (activated microglia), and X-34 ( $\beta$ -sheet-rich dense cores). APP/PS1x*Pld3*-WT  
711 (n=20), APP/PS1x*Pld3*-KO (n=19). B. Quantification of Iba1 localization within 15  $\mu$ m of the X-  
712 34+ dense core plaques (\*, p=0.03). C. Quantification of CD68 localization within 15  $\mu$ m of the  
713 dense plaques. D. Quantification of Iba1 and CD68 colocalization. Graphs represent mean  $\pm$   
714 SEM. Analyzed by two-tailed Student's *t* test with a ROUT outlier analysis (Q=1%).

715

716 **Figure 6: *PLD3* is enriched in specific microglia states in human brains.** A. Diagram of the  
717 study design for human brain sequencing. B. UMAP plot depicting segregation of human brain  
718 microglia into nine major subclusters, left. Bar plot of the log<sub>2</sub> fold change of *PLD3* by microglia  
719 subcluster, right. \*, p<0.05. C-D. Violin plot of *PLD3* expression from control (CO), sporadic AD  
720 (sAD), and *TREM2* risk variant carriers in homeostatic (Mic.0; C) and disease associated (Mic.1;  
721 D). E-G. Single cell RNAseq data obtained iTF-Microglia CROP-seq described previously [43].  
722 E. UMAP plot reveals 9 microglia clusters. F. Diagram of study design for iTF-Microglia, left.  
723 UMAP plot of *PLD3* expression, right. Cells are colored by the *PLD3* expression levels. G. Bar  
724 plot of the log<sub>2</sub> fold change of *PLD3* by microglia subcluster. \*, p<0.05.

725

726 **Supplemental Figure Legends**

727 **Supplemental Figure 1: Characterization of the *PLD3* p.A442A iPSC-derived neurons. A.**

728 Representative images of *PLD3* p.A442A and the corrected WT iPSCs stained for NANOG,

729 OCT4, SOX2, SSEA4, and TRA1-80. B. qPCR from known markers of pluripotency. C.

730 Karyotype. D. Sanger sequencing.

731

732 **Supplemental Figure 2: Generation of a *Pld3*-deficient amyloid mouse model. A. Mismatch**

733 detection assay. B. RNA activity validation. C. Breeding scheme for the *Pld3*-deficient mouse

734 with APP/PS1 mutant mice to develop a transgenic APP/PS1x*Pld3*-KO mouse line along with

735 APP/PS1x*Pld3*-WT littermate controls.

736

737 **Supplemental Figure 3: Loss of *Pld3* significantly increases plaque size without changing**

738 **plaque area.** A. Representative images of mice brain cross-sections stained for total A $\beta$  (HJ3.4)

739 with arrows specifying plaques (open arrows for WT; closed arrows for KO). APP/PS1x*Pld3*-WT

740 (n=20), APP/PS1x*Pld3*-KO (n=20). B-C. Quantification of average plaque size in the cortex (B)

741 and hippocampus (C). D-E. Quantification of average plaque count per mm<sup>2</sup> in the cortex (D)

742 and the hippocampus (E). F-G. Quantification of the plaque burden by the percentage of the

743 total area for the cortex (F) and the hippocampus (G). Graphs represent mean  $\pm$  SEM. \*,

744 p>0.05.

745

746 **Supplemental Figure 4: Loss of *Pld3* does not change dense core plaques. A.**

747 Representative images of mice brain cross sections stained with X-34 with arrows specifying



748 plaques (open arrows for WT; closed arrows for KO). APP/PS1x*Pld3*-WT (n=20),  
749 APP/PS1x*Pld3*-KO (n=20). B-C. Quantification of average plaque size in the cortex (B) and  
750 hippocampus (C). D-E. Quantification of average plaque count per mm<sup>2</sup> in the cortex (D) and  
751 hippocampus (E). F-G. The quantification of the plaque burden by the percentage of the total  
752 area for the cortex (F) and hippocampus (G). Graphs represent mean ± SEM.

753

754

755

756 **References**

- 757 [1] J. Hardy, D.J. Selkoe, The amyloid hypothesis of Alzheimer's disease: progress and  
758 problems on the road to therapeutics, *Science* 297(5580) (2002) 353-6.
- 759 [2] C.M. Karch, A.M. Goate, Alzheimer's disease risk genes and mechanisms of disease  
760 pathogenesis, *Biol Psychiatry* 77(1) (2015) 43-51.
- 761 [3] S.M. Neuner, J. Tcw, A.M. Goate, Genetic architecture of Alzheimer's disease, *Neurobiol Dis*  
762 143 (2020) 104976.
- 763 [4] C. Cruchaga, C.M. Karch, S.C. Jin, B.A. Benitez, Y. Cai, R. Guerreiro, O. Harari, J. Norton,  
764 J. Budde, S. Bertelsen, A.T. Jeng, B. Cooper, T. Skorupa, D. Carrell, D. Levitch, S. Hsu, J.  
765 Choi, M. Ryten, C. Sassi, J. Bras, R.J. Gibbs, D.G. Hernandez, M.K. Lupton, J. Powell, P.  
766 Forabosco, P.G. Ridge, C.D. Corcoran, J.T. Tschanz, M.C. Norton, R.G. Munger, C. Schmutz,  
767 M. Leary, F.Y. Demirci, M.N. Bamne, X. Wang, O.L. Lopez, M. Ganguli, C. Medway, J. Turton,  
768 J. Lord, A. Braae, I. Barber, K. Brown, U.K.C. Alzheimer's Research, P. Pastor, O. Lorenzo-  
769 Betancor, Z. Brkanac, E. Scott, E. Topol, K. Morgan, E. Rogaeva, A. Singleton, J. Hardy, M.I.  
770 Kamboh, P.S. George-Hyslop, N. Cairns, J.C. Morris, J.S.K. Kauwe, A.M. Goate, Rare coding  
771 variants in the phospholipase D3 gene confer risk for Alzheimer's disease, *Nature* 505(7484)  
772 (2014) 550-554.
- 773 [5] M. Osisami, W. Ali, M.A. Frohman, A role for phospholipase D3 in myotube formation, *PloS*  
774 *one* 7(3) (2012) e33341.
- 775 [6] A. Munck, C. Bohm, N.M. Seibel, Z. Hashemol Hosseini, W. Hampe, Hu-K4 is a ubiquitously  
776 expressed type 2 transmembrane protein associated with the endoplasmic reticulum, *The FEBS*  
777 *journal* 272(7) (2005) 1718-26.
- 778 [7] K.M. Pedersen, B. Finsen, J.E. Celis, N.A. Jensen, Expression of a novel murine  
779 phospholipase D homolog coincides with late neuronal development in the forebrain, *The*  
780 *Journal of biological chemistry* 273(47) (1998) 31494-504.

- 781 [8] J. Satoh, Y. Kino, Y. Yamamoto, N. Kawana, T. Ishida, Y. Saito, K. Arima, PLD3 is  
782 accumulated on neuritic plaques in Alzheimer's disease brains, *Alzheimers Res Ther* 6(9)  
783 (2014) 70.
- 784 [9] A.G. Nackenoff, T.J. Hohman, S.M. Neuner, C.S. Akers, N.C. Weitzel, A. Shostak, S.M.  
785 Ferguson, B. Mobley, D.A. Bennett, J.A. Schneider, A.L. Jefferson, C.C. Kaczorowski, M.S.  
786 Schrag, PLD3 is a neuronal lysosomal phospholipase D associated with beta-amyloid plaques  
787 and cognitive function in Alzheimer's disease, *PLoS Genet* 17(4) (2021) e1009406.
- 788 [10] C. Wang, H.F. Wang, M.S. Tan, Y. Liu, T. Jiang, D.Q. Zhang, L. Tan, J.T. Yu, I. Alzheimer's  
789 Disease Neuroimaging, Impact of Common Variations in PLD3 on Neuroimaging Phenotypes in  
790 Non-demented Elders, *Mol Neurobiol* 53(7) (2016) 4343-51.
- 791 [11] K. Takahashi, S. Yamanaka, Induction of pluripotent stem cells from mouse embryonic and  
792 adult fibroblast cultures by defined factors, *Cell* 126(4) (2006) 663-76.
- 793 [12] H. Ban, N. Nishishita, N. Fusaki, T. Tabata, K. Saeki, M. Shikamura, N. Takada, M. Inoue,  
794 M. Hasegawa, S. Kawamata, S. Nishikawa, Efficient generation of transgene-free human  
795 induced pluripotent stem cells (iPSCs) by temperature-sensitive Sendai virus vectors,  
796 *Proceedings of the National Academy of Sciences of the United States of America* 108(34)  
797 (2011) 14234-9.
- 798 [13] C.M. Karch, A.W. Kao, A. Karydas, K. Onanuga, R. Martinez, A. Argouarch, C. Wang, C.  
799 Huang, P.D. Sohn, K.R. Bowles, S. Spina, M.C. Silva, J.A. Marsh, S. Hsu, D.A. Pugh, N.  
800 Ghoshal, J. Norton, Y. Huang, S.E. Lee, W.W. Seeley, P. Theofilas, L.T. Grinberg, F. Moreno,  
801 K. McIlroy, B.F. Boeve, N.J. Cairns, J.F. Crary, S.J. Haggarty, J.K. Ichida, K.S. Kosik, B.L.  
802 Miller, L. Gan, A.M. Goate, S. Temple, G. Tau Consortium Stem Cell, A Comprehensive  
803 Resource for Induced Pluripotent Stem Cells from Patients with Primary Tauopathies, *Stem Cell*  
804 *Reports* 13(5) (2019) 939-955.
- 805 [14] S.W. Cho, S. Kim, J.M. Kim, J.S. Kim, Targeted genome engineering in human cells with  
806 the Cas9 RNA-guided endonuclease, *Nat Biotechnol* 31(3) (2013) 230-2.

- 807 [15] Z. Li, J.L. Del-Aguila, U. Dube, J. Budde, R. Martinez, K. Black, Q. Xiao, N.J. Cairns, N.  
808 Dominantly Inherited Alzheimer, J.D. Dougherty, J.M. Lee, J.C. Morris, R.J. Bateman, C.M.  
809 Karch, C. Cruchaga, O. Harari, Genetic variants associated with Alzheimer's disease confer  
810 different cerebral cortex cell-type population structure, *Genome Med* 10(1) (2018) 43.
- 811 [16] M. Allen, M.M. Carrasquillo, C. Funk, B.D. Heavner, F. Zou, C.S. Younkin, J.D. Burgess,  
812 H.-S. Chai, J. Crook, J.A. Eddy, H. Li, B. Logsdon, M.A. Peters, K.K. Dang, X. Wang, D. Serie,  
813 C. Wang, T. Nguyen, S. Lincoln, K. Malphrus, G. Bisceglia, M. Li, T.E. Golde, L.M. Mangravite,  
814 Y. Asmann, N.D. Price, R.C. Petersen, N.R. Graff-Radford, D.W. Dickson, S.G. Younkin, N.  
815 Ertekin-Taner, Human whole genome genotype and transcriptome data for Alzheimer's and  
816 other neurodegenerative diseases, *Scientific Data* 3(1) (2016) 160089.
- 817 [17] L. Brase, S.-F. You, J. del Aguila, Y. Dai, B.C. Novotny, C. Soriano-Tarraga, T. Dykstra,  
818 M.V. Fernandez, J.P. Budde, K. Bergmann, J.C. Morris, R.J. Bateman, R.J. Perrin, E. McDade,  
819 C. Xiong, A. Goate, M. Farlow, J.P. Chhatwal, P. Schofield, H. Chui, D.I.A. Network, G.T.  
820 Sutherland, J. Kipnis, C.M. Karch, B.A. Benitez, C. Cruchaga, O. Harari, A landscape of the  
821 genetic and cellular heterogeneity in Alzheimer disease, *medRxiv* (2021)  
822 2021.11.30.21267072.
- 823 [18] S. Da Mesquita, Z. Papadopoulos, T. Dykstra, L. Brase, F.G. Farias, M. Wall, H. Jiang, C.D.  
824 Kodira, K.A. de Lima, J. Herz, A. Louveau, D.H. Goldman, A.F. Salvador, S. Onengut-Gumuscu,  
825 E. Farber, N. Dabhi, T. Kennedy, M.G. Milam, W. Baker, I. Smirnov, S.S. Rich, N. Dominantly  
826 Inherited Alzheimer, B.A. Benitez, C.M. Karch, R.J. Perrin, M. Farlow, J.P. Chhatwal, D.M.  
827 Holtzman, C. Cruchaga, O. Harari, J. Kipnis, Meningeal lymphatics affect microglia responses  
828 and anti-Abeta immunotherapy, *Nature* 593(7858) (2021) 255-260.
- 829 [19] J.L. Jankowsky, D.J. Fadale, J. Anderson, G.M. Xu, V. Gonzales, N.A. Jenkins, N.G.  
830 Copeland, M.K. Lee, L.H. Younkin, S.L. Wagner, S.G. Younkin, D.R. Borchelt, Mutant  
831 presenilins specifically elevate the levels of the 42 residue beta-amyloid peptide in vivo:

832 evidence for augmentation of a 42-specific gamma secretase, *Hum Mol Genet* 13(2) (2004)  
833 159-70.

834 [20] Q. Xiao, P. Yan, X. Ma, H. Liu, R. Perez, A. Zhu, E. Gonzales, D.L. Tripoli, L. Czerniewski,  
835 A. Ballabio, J.R. Cirrito, A. Diwan, J.M. Lee, Neuronal-Targeted TFEB Accelerates Lysosomal  
836 Degradation of APP, Reducing Abeta Generation and Amyloid Plaque Pathogenesis, *J Neurosci*  
837 35(35) (2015) 12137-51.

838 [21] Q. Xiao, S.C. Gil, P. Yan, Y. Wang, S. Han, E. Gonzales, R. Perez, J.R. Cirrito, J.M. Lee,  
839 Role of phosphatidylinositol clathrin assembly lymphoid-myeloid leukemia (PICALM) in  
840 intracellular amyloid precursor protein (APP) processing and amyloid plaque pathogenesis, *The*  
841 *Journal of biological chemistry* 287(25) (2012) 21279-89.

842 [22] P. Yan, A.W. Bero, J.R. Cirrito, Q. Xiao, X. Hu, Y. Wang, E. Gonzales, D.M. Holtzman, J.-  
843 M. Lee, Characterizing the appearance and growth of amyloid plaques in APP/PS1 mice, *J*  
844 *Neurosci* 29(34) (2009) 10706-14.

845 [23] D.R. Borchelt, T. Ratovitski, J. van Lare, M.K. Lee, V. Gonzales, N.A. Jenkins, N.G.  
846 Copeland, D.L. Price, S.S. Sisodia, Accelerated amyloid deposition in the brains of transgenic  
847 mice coexpressing mutant presenilin 1 and amyloid precursor proteins, *Neuron* 19(4) (1997)  
848 939-45.

849 [24] Q. Xiao, P. Yan, X. Ma, H. Liu, R. Perez, A. Zhu, E. Gonzales, J.M. Burchett, D.R. Schuler,  
850 J.R. Cirrito, A. Diwan, J.M. Lee, Enhancing astrocytic lysosome biogenesis facilitates Abeta  
851 clearance and attenuates amyloid plaque pathogenesis, *J Neurosci* 34(29) (2014) 9607-20.

852 [25] J.R. Cirrito, P.C. May, M.A. O'Dell, J.W. Taylor, M. Parsadanian, J.W. Cramer, J.E. Audia,  
853 J.S. Nissen, K.R. Bales, S.M. Paul, R.B. DeMattos, D.M. Holtzman, In vivo assessment of brain  
854 interstitial fluid with microdialysis reveals plaque-associated changes in amyloid-beta  
855 metabolism and half-life, *The Journal of neuroscience : the official journal of the Society for*  
856 *Neuroscience* 23(26) (2003) 8844-53.

- 857 [26] J.R. Cirrito, K.A. Yamada, M.B. Finn, R.S. Sloviter, K.R. Bales, P.C. May, D.D. Schoepp,  
858 S.M. Paul, S. Mennerick, D.M. Holtzman, Synaptic activity regulates interstitial fluid amyloid-  
859 beta levels in vivo, *Neuron* 48(6) (2005) 913-22.
- 860 [27] J.C. Hettinger, H. Lee, G. Bu, D.M. Holtzman, J.R. Cirrito, AMPA-ergic regulation of  
861 amyloid-beta levels in an Alzheimer's disease mouse model, *Mol Neurodegener* 13(1) (2018)  
862 22.
- 863 [28] W. Farris, S.G. Schutz, J.R. Cirrito, G.M. Shankar, X. Sun, A. George, M.A. Leissring, D.M.  
864 Walsh, W.Q. Qiu, D.M. Holtzman, D.J. Selkoe, Loss of neprilysin function promotes amyloid  
865 plaque formation and causes cerebral amyloid angiopathy, *The American journal of pathology*  
866 171(1) (2007) 241-51.
- 867 [29] J.H. Roh, Y. Huang, A.W. Bero, T. Kasten, F.R. Stewart, R.J. Bateman, D.M. Holtzman,  
868 Disruption of the sleep-wake cycle and diurnal fluctuation of beta-amyloid in mice with  
869 Alzheimer's disease pathology, *Sci Transl Med* 4(150) (2012) 150ra122.
- 870 [30] H. Braak, E. Braak, Neuropathological staging of Alzheimer-related changes, *Acta*  
871 *Neuropathol* 82(4) (1991) 239-59.
- 872 [31] P. Fazzari, K. Horre, A.M. Arranz, C.S. Frigerio, T. Saito, T.C. Saido, B. De Strooper, *PLD3*  
873 gene and processing of APP, *Nature* 541(7638) (2017) E1-E2.
- 874 [32] J.M. Tarasoff-Conway, R.O. Carare, R.S. Osorio, L. Glodzik, T. Butler, E. Fieremans, L.  
875 Axel, H. Rusinek, C. Nicholson, B.V. Zlokovic, B. Frangione, K. Blennow, J. Menard, H.  
876 Zetterberg, T. Wisniewski, M.J. de Leon, Clearance systems in the brain-implications for  
877 Alzheimer disease, *Nat Rev Neurol* 11(8) (2015) 457-70.
- 878 [33] K.G. Mawuenyega, W. Sigurdson, V. Ovod, L. Munsell, T. Kasten, J.C. Morris, K.E.  
879 Yarasheski, R.J. Bateman, Decreased clearance of CNS beta-amyloid in Alzheimer's disease,  
880 *Science* 330(6012) (2010) 1774.

- 881 [34] A.W. Bero, P. Yan, J.H. Roh, J.R. Cirrito, F.R. Stewart, M.E. Raichle, J.M. Lee, D.M.  
882 Holtzman, Neuronal activity regulates the regional vulnerability to amyloid-beta deposition, *Nat*  
883 *Neurosci* 14(6) (2011) 750-6.
- 884 [35] C.M. Vander Zanden, L. Wampler, I. Bowers, E.B. Watkins, J. Majewski, E.Y. Chi, Fibrillar  
885 and Nonfibrillar Amyloid Beta Structures Drive Two Modes of Membrane-Mediated Toxicity,  
886 *Langmuir* 35(48) (2019) 16024-16036.
- 887 [36] Y. Wang, T.K. Ulland, J.D. Ulrich, W. Song, J.A. Tzaferis, J.T. Hole, P. Yuan, T.E. Mahan,  
888 Y. Shi, S. Gilfillan, M. Cella, J. Grutzendler, R.B. DeMattos, J.R. Cirrito, D.M. Holtzman, M.  
889 Colonna, TREM2-mediated early microglial response limits diffusion and toxicity of amyloid  
890 plaques, *J Exp Med* 213(5) (2016) 667-75.
- 891 [37] J.D. Ulrich, T.K. Ulland, T.E. Mahan, S. Nystrom, K.P. Nilsson, W.M. Song, Y. Zhou, M.  
892 Reinartz, S. Choi, H. Jiang, F.R. Stewart, E. Anderson, Y. Wang, M. Colonna, D.M. Holtzman,  
893 ApoE facilitates the microglial response to amyloid plaque pathology, *J Exp Med* 215(4) (2018)  
894 1047-1058.
- 895 [38] T.K. Ulland, W.M. Song, S.C. Huang, J.D. Ulrich, A. Sergushichev, W.L. Beatty, A.A.  
896 Loboda, Y. Zhou, N.J. Cairns, A. Kambal, E. Loginicheva, S. Gilfillan, M. Cella, H.W. Virgin,  
897 E.R. Unanue, Y. Wang, M.N. Artyomov, D.M. Holtzman, M. Colonna, TREM2 Maintains  
898 Microglial Metabolic Fitness in Alzheimer's Disease, *Cell* 170(4) (2017) 649-663 e13.
- 899 [39] J.D. Ulrich, M.B. Finn, Y. Wang, A. Shen, T.E. Mahan, H. Jiang, F.R. Stewart, L. Piccio, M.  
900 Colonna, D.M. Holtzman, Altered microglial response to Abeta plaques in APPPS1-21 mice  
901 heterozygous for TREM2, *Mol Neurodegener* 9 (2014) 20.
- 902 [40] S. Krasemann, C. Madore, R. Cialic, C. Baufeld, N. Calcagno, R. El Fatimy, L. Beckers, E.  
903 O'Loughlin, Y. Xu, Z. Fanek, D.J. Greco, S.T. Smith, G. Tweet, Z. Humulock, T. Zrzavy, P.  
904 Conde-Sanroman, M. Gacias, Z. Weng, H. Chen, E. Tjon, F. Mazaheri, K. Hartmann, A. Madi,  
905 J.D. Ulrich, M. Glatzel, A. Worthmann, J. Heeren, B. Budnik, C. Lemere, T. Ikezu, F.L. Heppner,  
906 V. Litvak, D.M. Holtzman, H. Lassmann, H.L. Weiner, J. Ochoa, C. Haass, O. Butovsky, The

907 TREM2-APOE Pathway Drives the Transcriptional Phenotype of Dysfunctional Microglia in  
908 Neurodegenerative Diseases, *Immunity* 47(3) (2017) 566-581 e9.

909 [41] H. Keren-Shaul, A. Spinrad, A. Weiner, O. Matcovitch-Natan, R. Dvir-Szternfeld, T.K.  
910 Ulland, E. David, K. Baruch, D. Lara-Astaiso, B. Toth, S. Itzkovitz, M. Colonna, M. Schwartz, I.  
911 Amit, A Unique Microglia Type Associated with Restricting Development of Alzheimer's Disease,  
912 *Cell* 169(7) (2017) 1276-1290 e17.

913 [42] C. Sala Frigerio, L. Wolfs, N. Fattorelli, N. Thrupp, I. Voytyuk, I. Schmidt, R. Mancuso, W.T.  
914 Chen, M.E. Woodbury, G. Srivastava, T. Moller, E. Hudry, S. Das, T. Saido, E. Karran, B.  
915 Hyman, V.H. Perry, M. Fiers, B. De Strooper, The Major Risk Factors for Alzheimer's Disease:  
916 Age, Sex, and Genes Modulate the Microglia Response to Abeta Plaques, *Cell Rep* 27(4)  
917 (2019) 1293-1306 e6.

918 [43] N.M. Dräger, S.M. Sattler, C.T.-L. Huang, O.M. Teter, K. Leng, S.H. Hashemi, J. Hong,  
919 C.D. Clelland, L. Zhan, L. Kodama, A.B. Singleton, M.A. Nalls, J. Ichida, M.E. Ward, F. Faghri,  
920 L. Gan, M. Kampmann, A CRISPRi/a platform in iPSC-derived microglia uncovers regulators of  
921 disease states, *bioRxiv* (2021) 2021.06.16.448639.

922 [44] C.M. Karch, A.M. Goate, Alzheimer's Disease Risk Genes and Mechanisms of Disease  
923 Pathogenesis, *Biol Psychiatry* (2014).

924 [45] R. Sims, S.J. van der Lee, A.C. Naj, C. Bellenguez, N. Badarinarayan, J. Jakobsdottir, B.W.  
925 Kunkle, A. Boland, R. Raybould, J.C. Bis, E.R. Martin, B. Grenier-Boley, S. Heilmann-  
926 Heimbach, V. Chouraki, A.B. Kuzma, K. Sleegers, M. Vronskaya, A. Ruiz, R.R. Graham, R.  
927 Olaso, P. Hoffmann, M.L. Grove, B.N. Vardarajan, M. Hiltunen, M.M. Nothen, C.C. White, K.L.  
928 Hamilton-Nelson, J. Epelbaum, W. Maier, S.H. Choi, G.W. Beecham, C. Dulary, S. Herms, A.V.  
929 Smith, C.C. Funk, C. Derbois, A.J. Forstner, S. Ahmad, H. Li, D. Bacq, D. Harold, C.L.  
930 Satizabal, O. Valladares, A. Squassina, R. Thomas, J.A. Brody, L. Qu, P. Sanchez-Juan, T.  
931 Morgan, F.J. Wolters, Y. Zhao, F.S. Garcia, N. Denning, M. Fornage, J. Malamon, M.C.D.  
932 Naranjo, E. Majounie, T.H. Mosley, B. Dombroski, D. Wallon, M.K. Lupton, J. Dupuis, P.



933 Whitehead, L. Fratiglioni, C. Medway, X. Jian, S. Mukherjee, L. Keller, K. Brown, H. Lin, L.B.  
934 Cantwell, F. Panza, B. McGuinness, S. Moreno-Grau, J.D. Burgess, V. Solfrizzi, P. Proitsi, H.H.  
935 Adams, M. Allen, D. Seripa, P. Pastor, L.A. Cupples, N.D. Price, D. Hannequin, A. Frank-  
936 Garcia, D. Levy, P. Chakrabarty, P. Caffarra, I. Giegling, A.S. Beiser, V. Giedraitis, H. Hampel,  
937 M.E. Garcia, X. Wang, L. Lannfelt, P. Mecocci, G. Eiriksdottir, P.K. Crane, F. Pasquier, V.  
938 Boccardi, I. Henandez, R.C. Barber, M. Scherer, L. Tarraga, P.M. Adams, M. Leber, Y. Chen,  
939 M.S. Albert, S. Riedel-Heller, V. Emilsson, D. Beekly, A. Braae, R. Schmidt, D. Blacker, C.  
940 Masullo, H. Schmidt, R.S. Doody, G. Spalletta, W.T. Longstreth, Jr., T.J. Fairchild, P. Bossu,  
941 O.L. Lopez, M.P. Frosch, E. Sacchinelli, B. Ghetti, Q. Yang, R.M. Huebinger, F. Jessen, S. Li,  
942 M.I. Kamboh, J. Morris, O. Sotolongo-Grau, M.J. Katz, C. Corcoran, M. Dunstan, A. Braddel, C.  
943 Thomas, A. Meggy, R. Marshall, A. Gerrish, J. Chapman, M. Aguilar, S. Taylor, M. Hill, M.D.  
944 Fairen, A. Hodges, B. Vellas, H. Soininen, I. Kloszewska, M. Daniilidou, J. Uphill, Y. Patel, J.T.  
945 Hughes, J. Lord, J. Turton, A.M. Hartmann, R. Cecchetti, C. Fenoglio, M. Serpente, M. Arcaro,  
946 C. Caltagirone, M.D. Orfei, A. Ciaramella, S. Pichler, M. Mayhaus, W. Gu, A. Lleo, J. Fortea, R.  
947 Blesa, I.S. Barber, K. Brookes, C. Cupidi, R.G. Maletta, D. Carrell, S. Sorbi, S. Moebus, M.  
948 Urbano, A. Pilotto, J. Kornhuber, P. Bosco, S. Todd, D. Craig, J. Johnston, M. Gill, B. Lawlor, A.  
949 Lynch, N.C. Fox, J. Hardy, A. Consortium, R.L. Albin, L.G. Apostolova, S.E. Arnold, S. Asthana,  
950 C.S. Atwood, C.T. Baldwin, L.L. Barnes, S. Barral, T.G. Beach, J.T. Becker, E.H. Bigio, T.D.  
951 Bird, B.F. Boeve, J.D. Bowen, A. Boxer, J.R. Burke, J.M. Burns, J.D. Buxbaum, N.J. Cairns, C.  
952 Cao, C.S. Carlson, C.M. Carlsson, R.M. Carney, M.M. Carrasquillo, S.L. Carroll, C.C. Diaz, H.C.  
953 Chui, D.G. Clark, D.H. Cribbs, E.A. Crocco, C. DeCarli, M. Dick, R. Duara, D.A. Evans, K.M.  
954 Faber, K.B. Fallon, D.W. Fardo, M.R. Farlow, S. Ferris, T.M. Foroud, D.R. Galasko, M. Gearing,  
955 D.H. Geschwind, J.R. Gilbert, N.R. Graff-Radford, R.C. Green, J.H. Growdon, R.L. Hamilton,  
956 L.E. Harrell, L.S. Honig, M.J. Huentelman, C.M. Hulette, B.T. Hyman, G.P. Jarvik, E. Abner,  
957 L.W. Jin, G. Jun, A. Karydas, J.A. Kaye, R. Kim, N.W. Kowall, J.H. Kramer, F.M. LaFerla, J.J.  
958 Lah, J.B. Leverenz, A.I. Levey, G. Li, A.P. Lieberman, K.L. Lunetta, C.G. Lyketsos, D.C.

959 Marson, F. Martiniuk, D.C. Mash, E. Masliah, W.C. McCormick, S.M. McCurry, A.N. McDavid,  
960 A.C. McKee, M. Mesulam, B.L. Miller, C.A. Miller, J.W. Miller, J.C. Morris, J.R. Murrell, A.J.  
961 Myers, S. O'Bryant, J.M. Olichney, V.S. Pankratz, J.E. Parisi, H.L. Paulson, W. Perry, E.  
962 Peskind, A. Pierce, W.W. Poon, H. Potter, J.F. Quinn, A. Raj, M. Raskind, B. Reisberg, C. Reitz,  
963 J.M. Ringman, E.D. Roberson, E. Rogaeva, H.J. Rosen, R.N. Rosenberg, M.A. Sager, A.J.  
964 Saykin, J.A. Schneider, L.S. Schneider, W.W. Seeley, A.G. Smith, J.A. Sonnen, S. Spina, R.A.  
965 Stern, R.H. Swerdlow, R.E. Tanzi, T.A. Thornton-Wells, J.Q. Trojanowski, J.C. Troncoso, V.M.  
966 Van Deerlin, L.J. Van Eldik, H.V. Vinters, J.P. Vonsattel, S. Weintraub, K.A. Welsh-Bohmer,  
967 K.C. Wilhelmsen, J. Williamson, T.S. Wingo, R.L. Woltjer, C.B. Wright, C.E. Yu, L. Yu, F.  
968 Garzia, F. Golamaully, G. Septier, S. Engelborghs, R. Vandenberghe, P.P. De Deyn, C.M.  
969 Fernandez, Y.A. Benito, H. Thonberg, C. Forsell, L. Lilius, A. Kinhult-Stahlbom, L. Kilander, R.  
970 Brundin, L. Concari, S. Helisalimi, A.M. Koivisto, A. Haapasalo, V. Dermecourt, N. Fievet, O.  
971 Hanon, C. Dufouil, A. Brice, K. Ritchie, B. Dubois, J.J. Himali, C.D. Keene, J. Tschanz, A.L.  
972 Fitzpatrick, W.A. Kukull, M. Norton, T. Aspelund, E.B. Larson, R. Munger, J.I. Rotter, R.B.  
973 Lipton, M.J. Bullido, A. Hofman, T.J. Montine, E. Coto, E. Boerwinkle, R.C. Petersen, V.  
974 Alvarez, F. Rivadeneira, E.M. Reiman, M. Gallo, C.J. O'Donnell, J.S. Reisch, A.C. Bruni, D.R.  
975 Royall, M. Dichgans, M. Sano, D. Galimberti, P. St George-Hyslop, E. Scarpini, D.W. Tsuang,  
976 M. Mancuso, U. Bonuccelli, A.R. Winslow, A. Daniele, C.K. Wu, C.A.E. Gerad/Perades, O.  
977 Peters, B. Nacmias, M. Riemenschneider, R. Heun, C. Brayne, D.C. Rubinsztein, J. Bras, R.  
978 Guerreiro, A. Al-Chalabi, C.E. Shaw, J. Collinge, D. Mann, M. Tsolaki, J. Clarimon, R. Sussams,  
979 S. Lovestone, M.C. O'Donovan, M.J. Owen, T.W. Behrens, S. Mead, A.M. Goate, A.G.  
980 Uitterlinden, C. Holmes, C. Cruchaga, M. Ingelsson, D.A. Bennett, J. Powell, T.E. Golde, C.  
981 Graff, P.L. De Jager, K. Morgan, N. Ertekin-Taner, O. Combarros, B.M. Psaty, P. Passmore,  
982 S.G. Younkin, C. Berr, V. Gudnason, D. Rujescu, D.W. Dickson, J.F. Dartigues, A.L. DeStefano,  
983 S. Ortega-Cubero, H. Hakonarson, D. Champion, M. Boada, J.K. Kauwe, L.A. Farrer, C. Van  
984 Broeckhoven, M.A. Ikram, L. Jones, J.L. Haines, C. Tzourio, L.J. Launer, V. Escott-Price, R.

985 Mayeux, J.F. Deleuze, N. Amin, P.A. Holmans, M.A. Pericak-Vance, P. Amouyel, C.M. van  
986 Duijn, A. Ramirez, L.S. Wang, J.C. Lambert, S. Seshadri, J. Williams, G.D. Schellenberg, Rare  
987 coding variants in PLCG2, ABI3, and TREM2 implicate microglial-mediated innate immunity in  
988 Alzheimer's disease, *Nat Genet* 49(9) (2017) 1373-1384.

989 [46] S. Hsu, A.A. Pimenova, K. Hayes, J.A. Villa, M.J. Rosene, M. Jere, A.M. Goate, C.M.  
990 Karch, Systematic validation of variants of unknown significance in APP, PSEN1 and PSEN2,  
991 *Neurobiol Dis* 139 (2020) 104817.

992 [47] S. Hsu, B.A. Gordon, R. Hornbeck, J.B. Norton, D. Levitch, A. Louden, E. Ziegemeier, R.  
993 Laforce, Jr., J. Chhatwal, G.S. Day, E. McDade, J.C. Morris, A.M. Fagan, T.L.S. Benzinger,  
994 A.M. Goate, C. Cruchaga, R.J. Bateman, N. Dominantly Inherited Alzheimer, C.M. Karch,  
995 Discovery and validation of autosomal dominant Alzheimer's disease mutations, *Alzheimers Res*  
996 *Ther* 10(1) (2018) 67.

997 [48] A.S. Mukadam, S.Y. Breusegem, M.N.J. Seaman, Analysis of novel endosome-to-Golgi  
998 retrieval genes reveals a role for PLD3 in regulating endosomal protein sorting and amyloid  
999 precursor protein processing, *Cell Mol Life Sci* 75(14) (2018) 2613-2625.

1000 [49] A.C. Gonzalez, M. Schweizer, S. Jagdmann, C. Bernreuther, T. Reinheckel, P. Saftig, M.  
1001 Damme, Unconventional Trafficking of Mammalian Phospholipase D3 to Lysosomes, *Cell Rep*  
1002 22(4) (2018) 1040-1053.

1003 [50] L.C. Walker, Abeta Plaques, *Free Neuropathol* 1 (2020).

1004 [51] A.R. Ladiwala, J. Litt, R.S. Kane, D.S. Aucoin, S.O. Smith, S. Ranjan, J. Davis, W.E. Van  
1005 Nostrand, P.M. Tessier, Conformational differences between two amyloid beta oligomers of  
1006 similar size and dissimilar toxicity, *J Biol Chem* 287(29) (2012) 24765-73.

1007 [52] Y. Zhang, K. Chen, S.A. Sloan, M.L. Bennett, A.R. Scholze, S. O'Keefe, H.P. Phatnani, P.  
1008 Guarnieri, C. Caneda, N. Ruderisch, S. Deng, S.A. Liddelow, C. Zhang, R. Daneman, T.  
1009 Maniatis, B.A. Barres, J.Q. Wu, An RNA-Sequencing Transcriptome and Splicing Database of  
1010 Glia, Neurons, and Vascular Cells of the Cerebral Cortex, *J Neurosci* 34(36) (2014) 11929-47.

1011 [53] T.D. Troutman, E. Kofman, C.K. Glass, Exploiting dynamic enhancer landscapes to decode  
1012 macrophage and microglia phenotypes in health and disease, *Mol Cell* 81(19) (2021) 3888-  
1013 3903.

1014 [54] W.S. Liang, T. Dunckley, T.G. Beach, A. Grover, D. Mastroeni, D.G. Walker, R.J. Caselli,  
1015 W.A. Kukull, D. McKeel, J.C. Morris, C. Hulette, D. Schmechel, G.E. Alexander, E.M. Reiman, J.  
1016 Rogers, D.A. Stephan, Gene expression profiles in anatomically and functionally distinct regions  
1017 of the normal aged human brain, *Physiol Genomics* 28(3) (2007) 311-22.

1018

## Figure 1

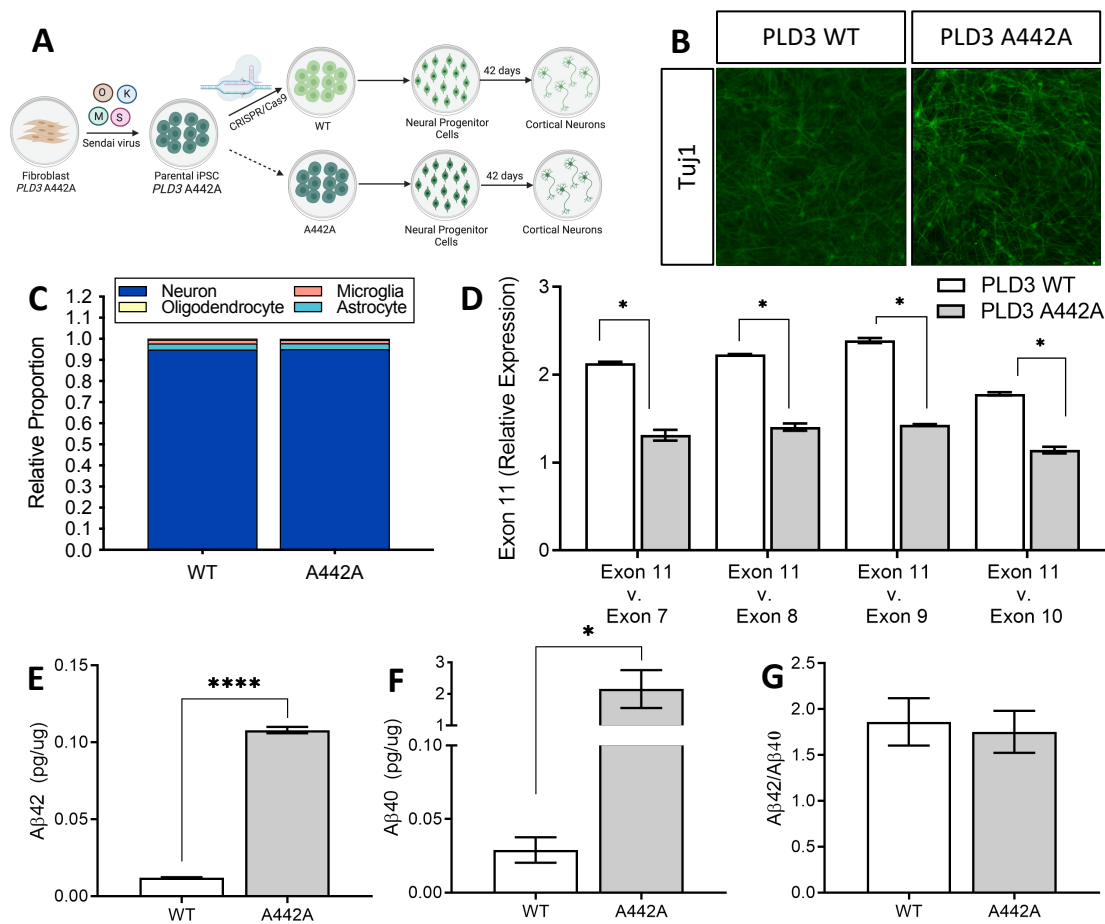


## Figure 2

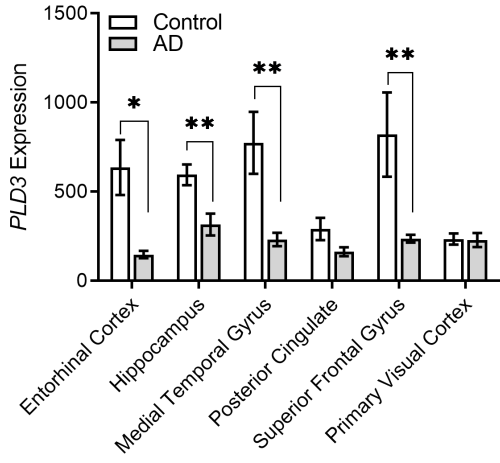


## Figure 3

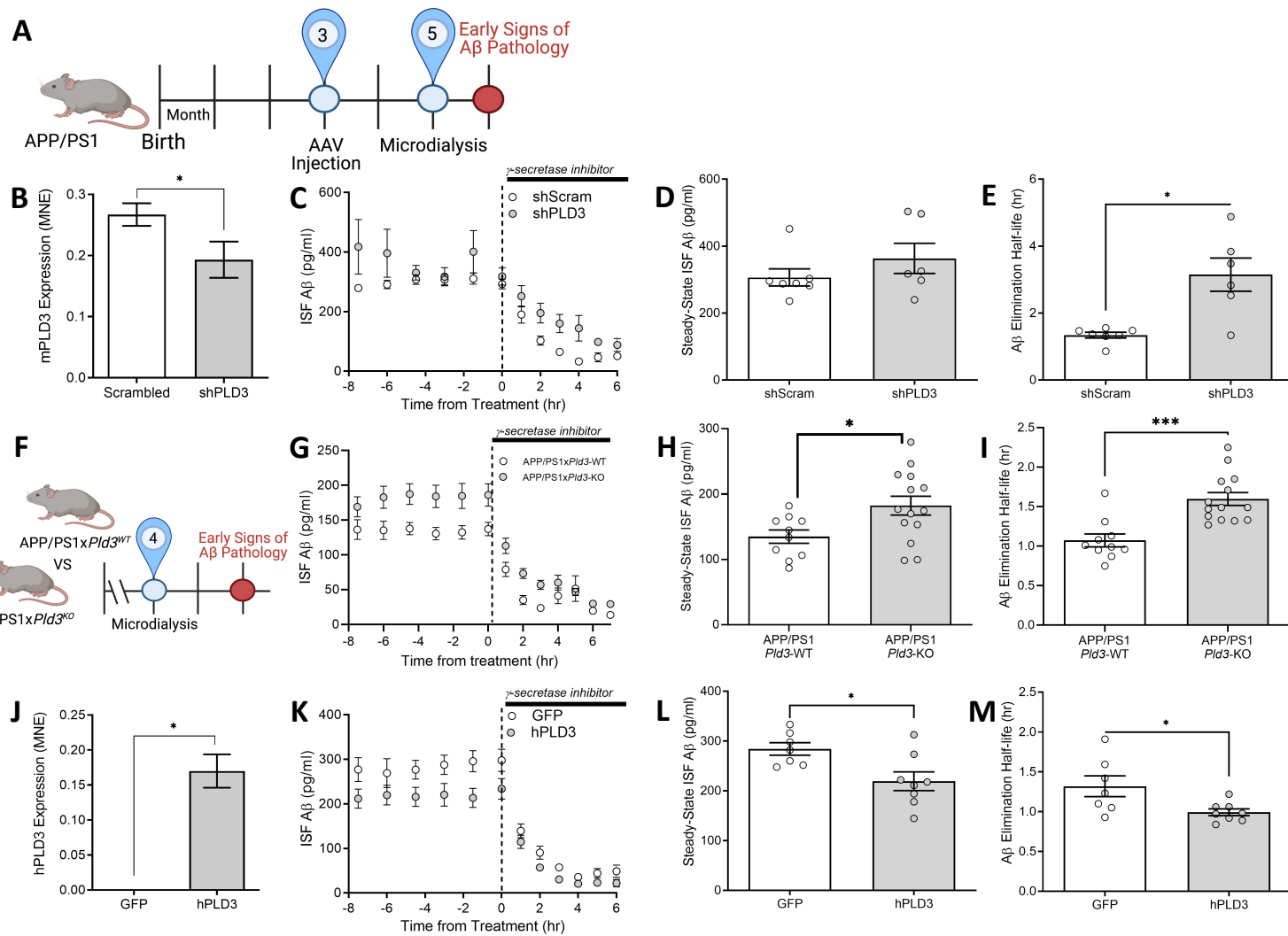


## Figure 4

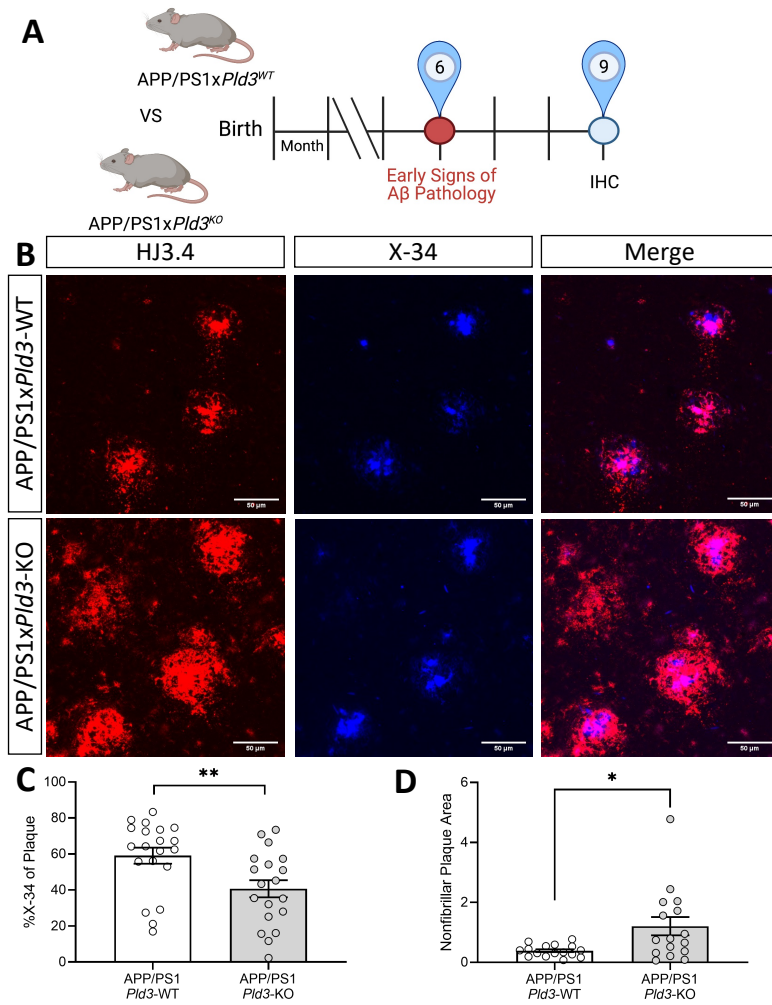




## Figure 5

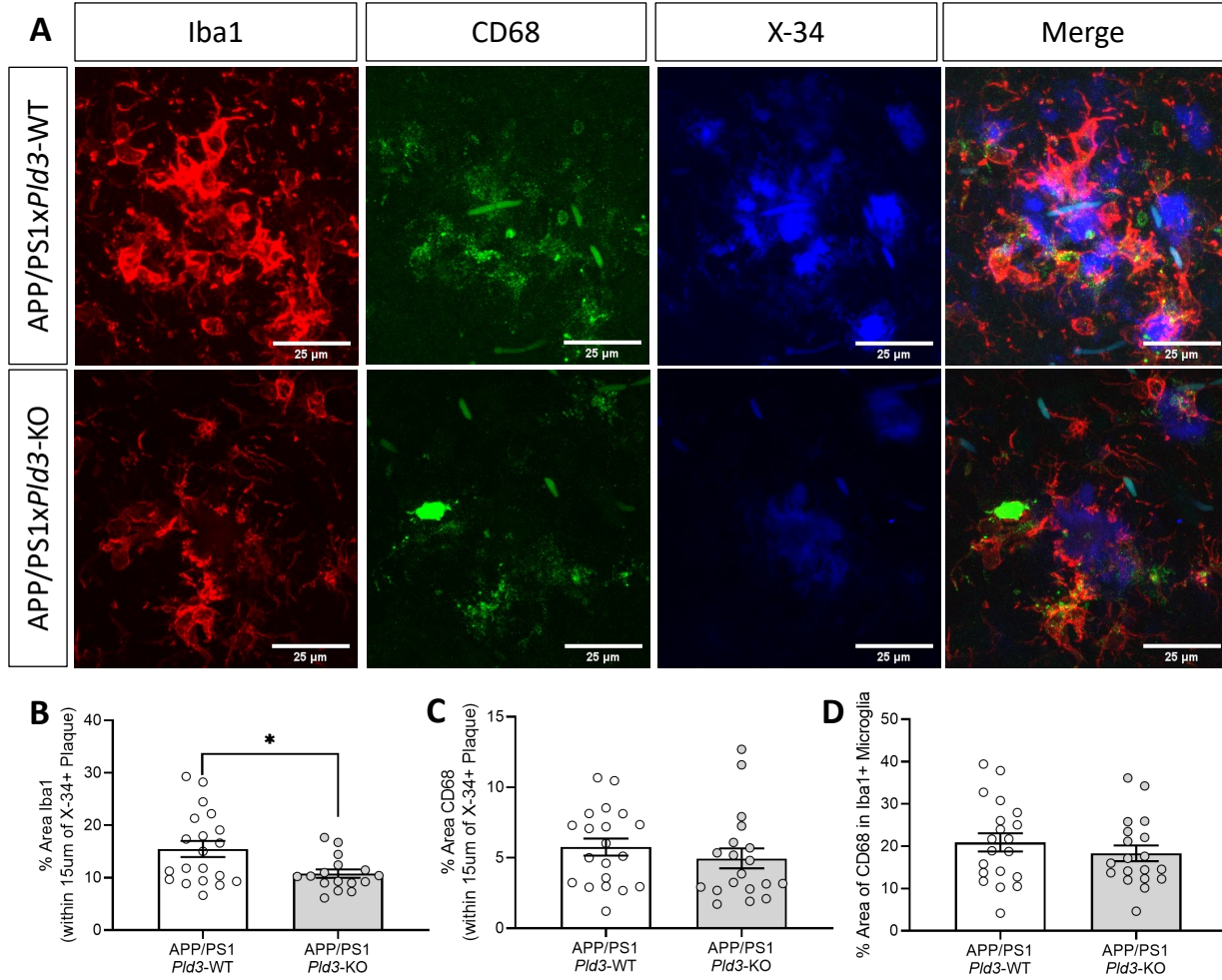
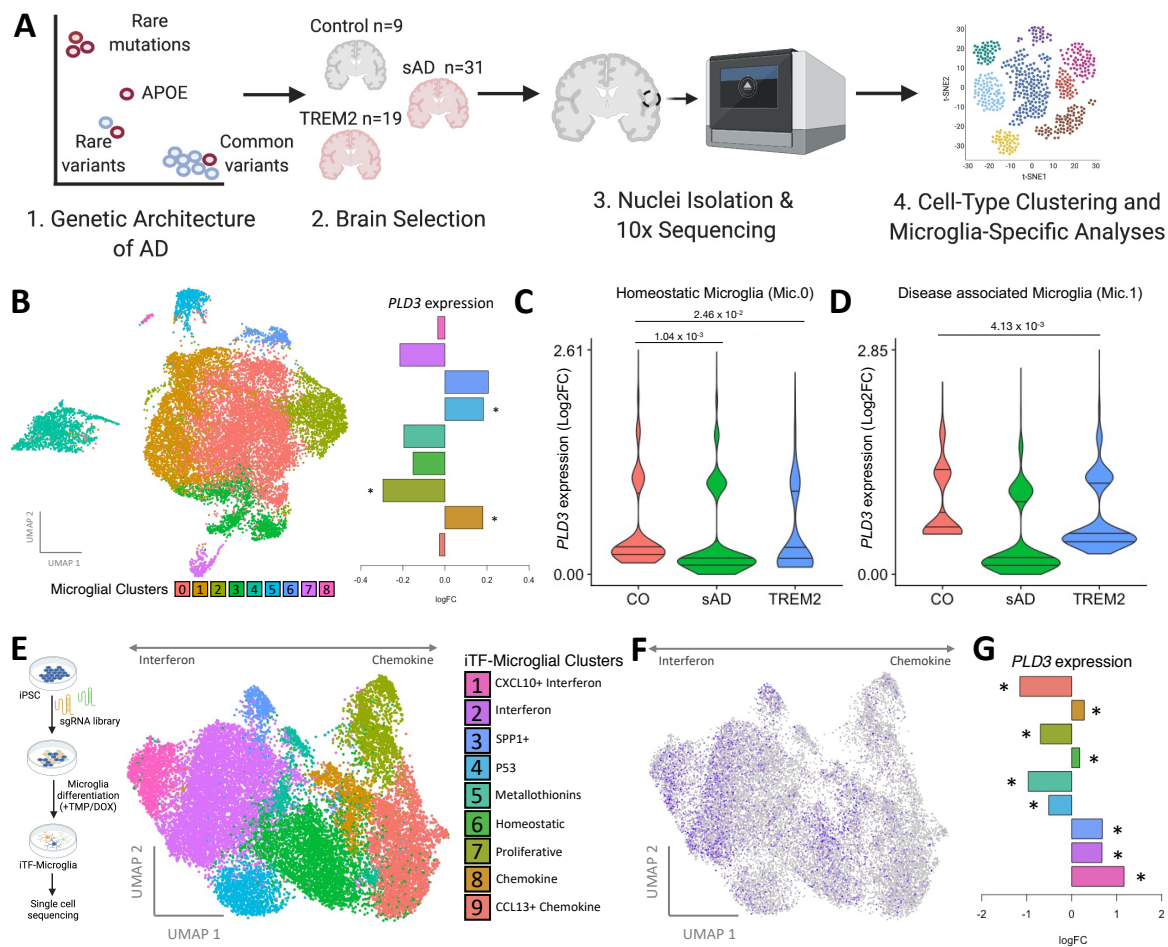
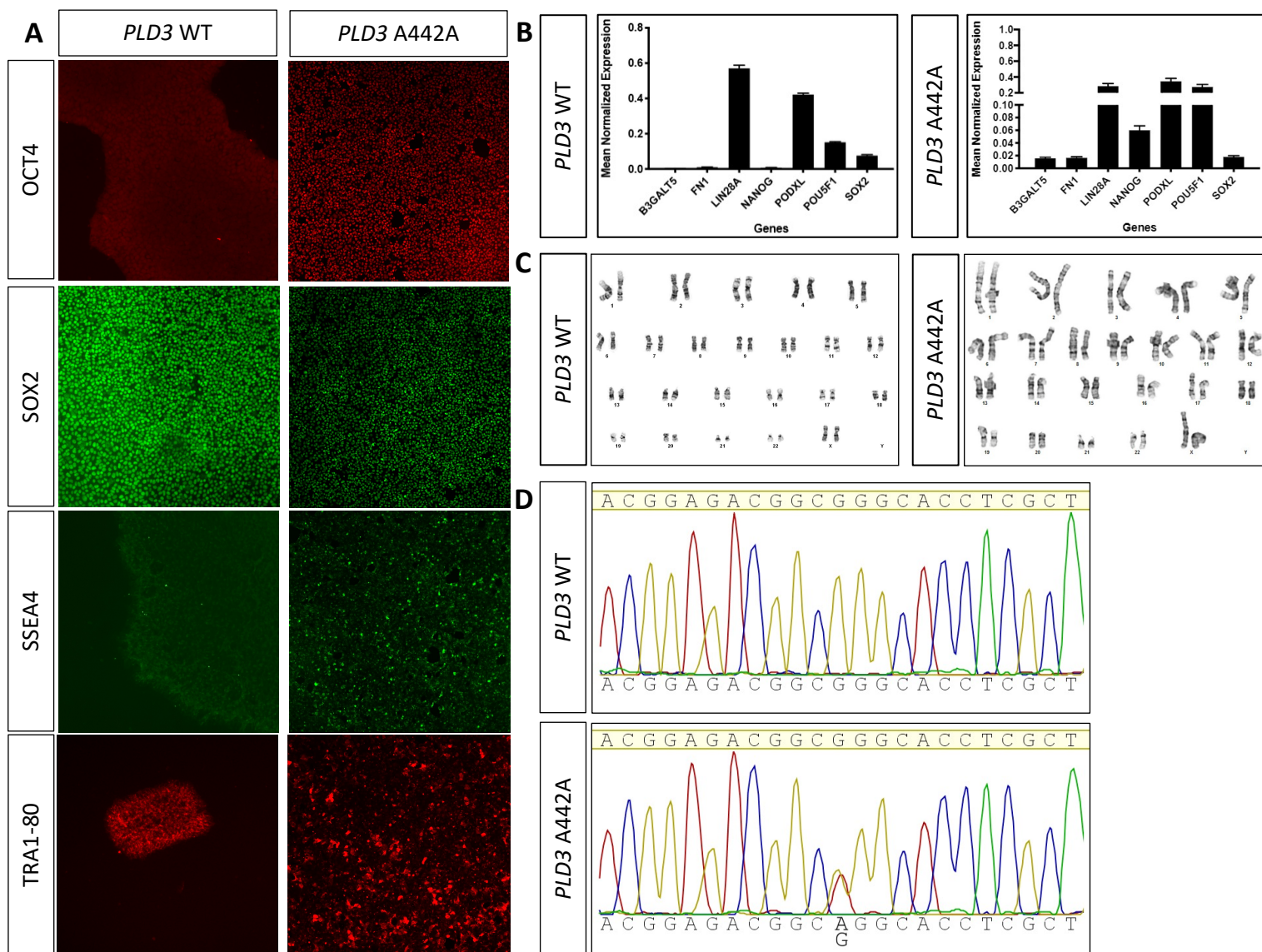


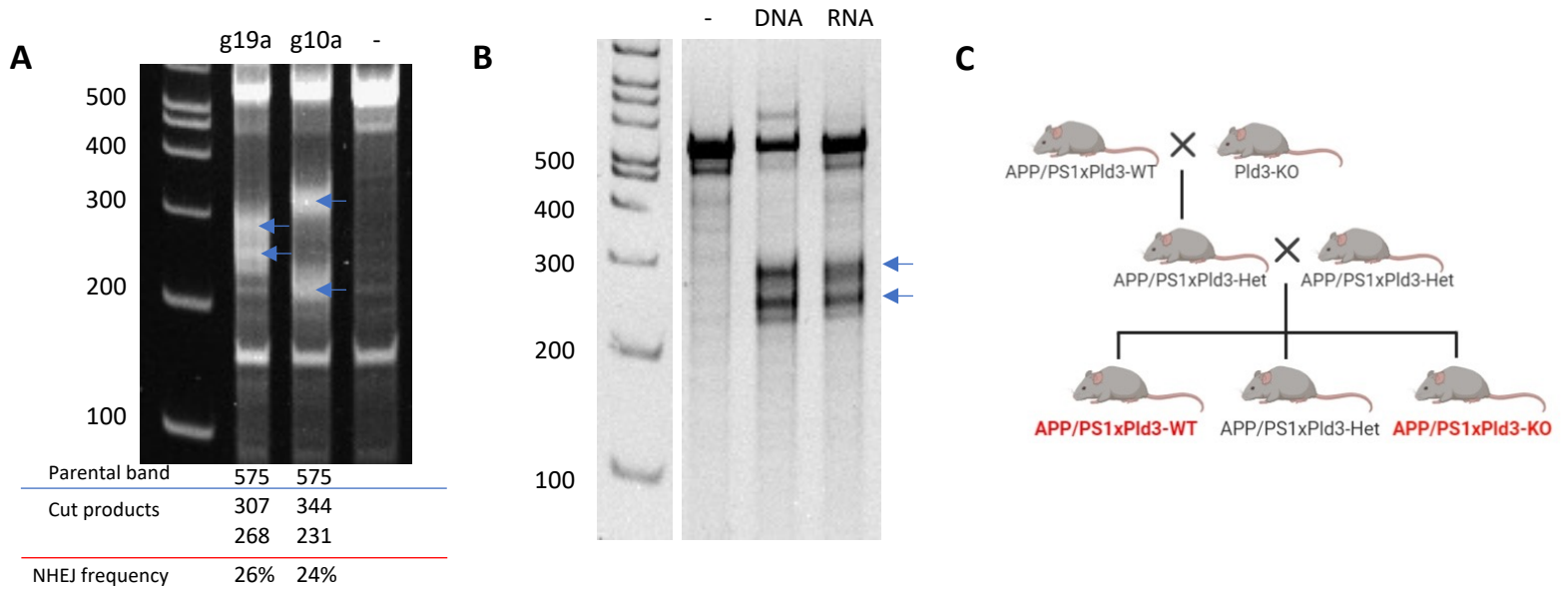
## Figure 6



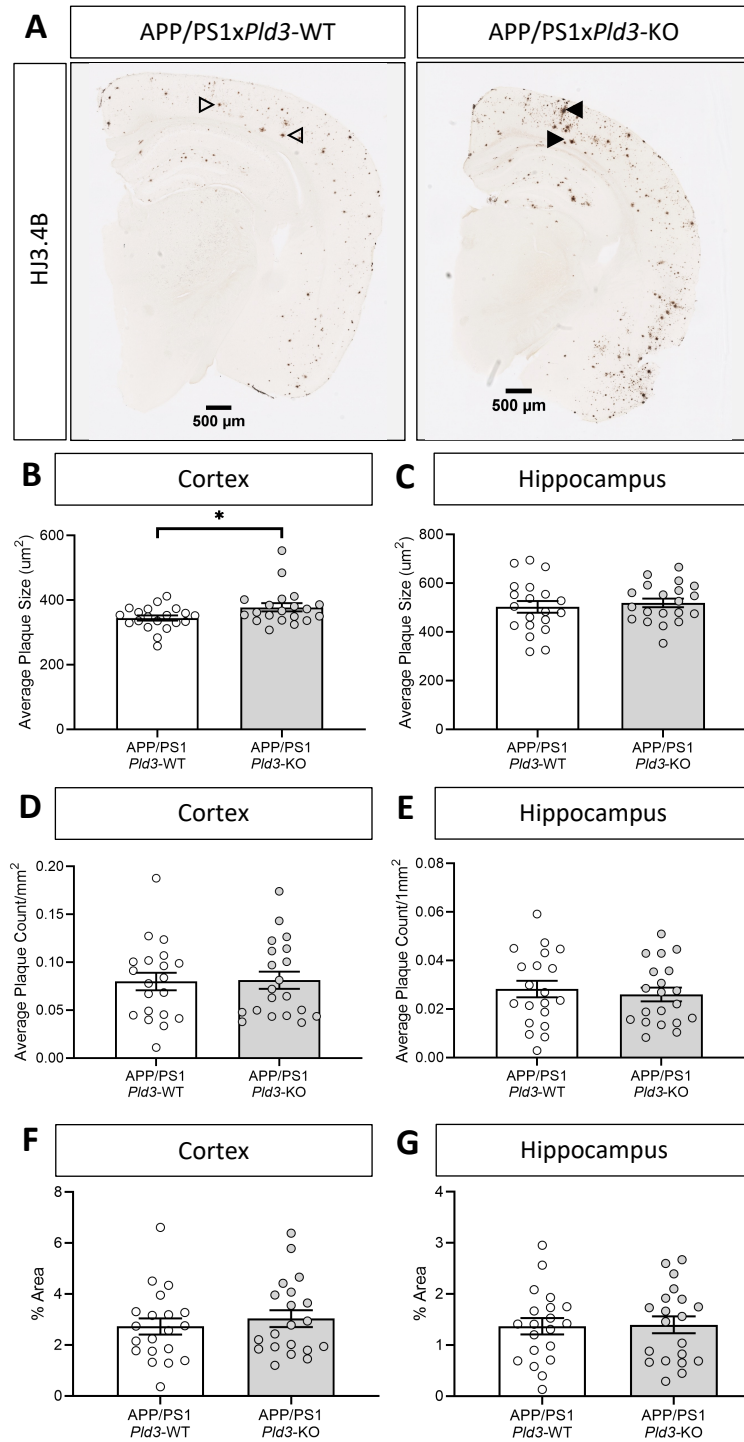
# Supplemental Figure 1



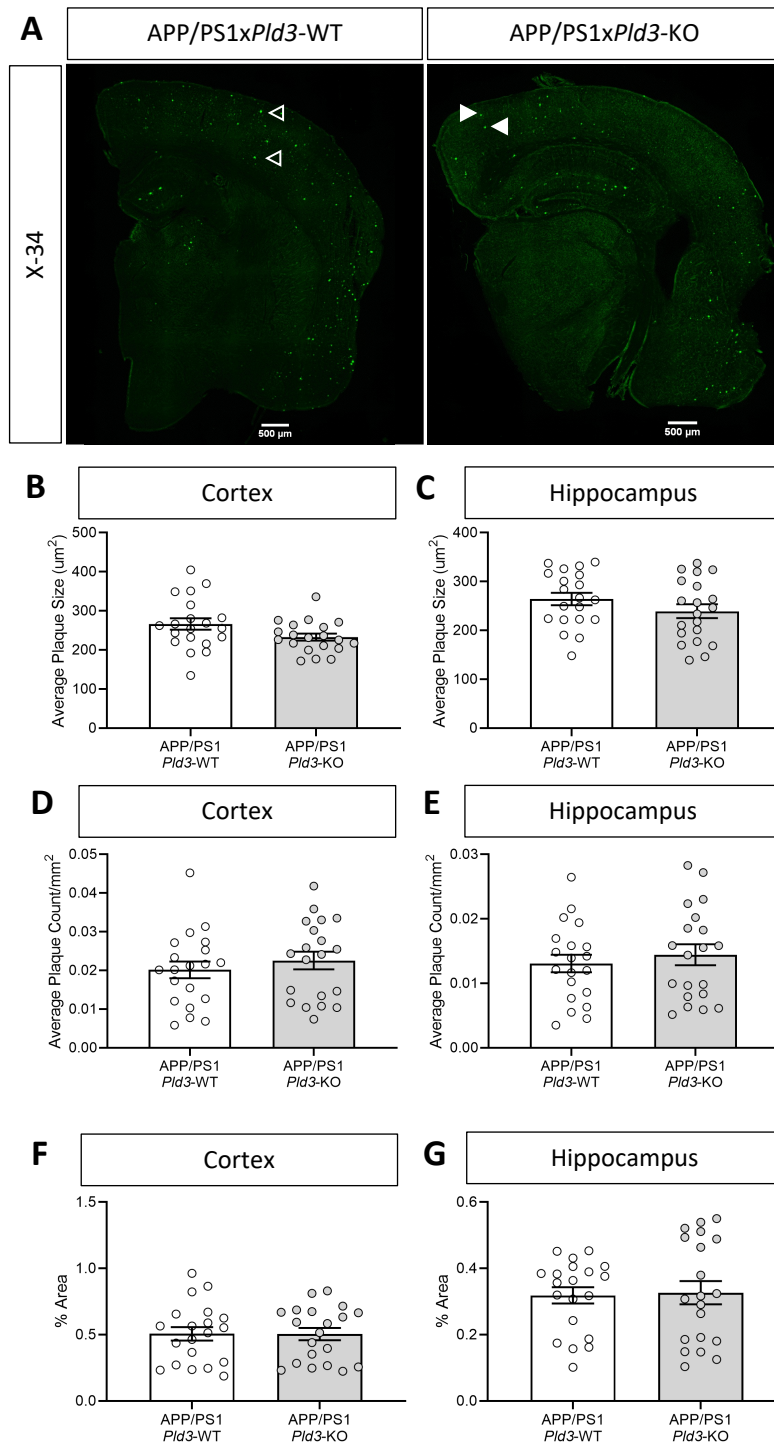
## Supplemental Figure 2



# Supplemental Figure 3



## Supplemental Figure 4



## Supplemental Tables

	Total Number	Sex (% male)	Mean Age at Death (years)	APOE4	Mean Postmortem Interval (years)
Controls	9	33%	90	11%	10.9
sAD	31	45%	81	54%	11.9

Cluster Name	LogFC	z-score	p-value	BH corrected p-value
Mic.0	-0.0262225	-0.6410652	5.21E-01	7.32E-01
Mic.1	0.1800801	4.19659881	2.71E-05	2.86E-04
Mic.2	-0.2949385	-4.7275062	2.27E-06	1.26E-04
Mic.3	-0.1519921	-1.274392	2.03E-01	5.14E-01
Mic.4	-0.1953743	-1.718988	8.56E-02	2.51E-01
Mic.5	0.1829342	1.98158159	4.75E-02	1.75E-01
Mic.6	0.20610645	1.89898926	5.76E-02	1.96E-01
Mic.7	-0.2146737	-1.3839443	1.66E-01	4.50E-01
Mic.8	-0.0345632	-0.1138777	9.09E-01	9.99E-01

Comparison	LogFC	z-score	p-value	BH corrected p-value	Subcluster
sAD vs CO	-0.4017806	-3.2799941	1.04E-03	1.43E-01	Mic.0
TREM2 vs CO	-0.2766865	-2.247029	2.46E-02	3.91E-01	Mic.0
sAD vs CO	-0.3455155	-1.8251283	6.80E-02	1.00E+00	Mic.1
TREM2 vs CO	-0.4217827	-2.8679334	4.13E-03	3.21E-01	Mic.1

Cluster Name	Estimate	Std. Error	z value	Pr(> z )
cluster 1	1.163684751	0.079301251	14.67422936	9.43E-49
cluster 2	0.673908846	0.041847298	16.10399883	2.39E-58
cluster 3	0.679645559	0.12978185	5.236830561	1.63E-07
cluster 4	-0.511168775	0.081414971	-6.278559975	3.42E-10
cluster 5	-0.966514606	0.105007855	-9.204212437	3.44E-20
cluster 6	0.178261422	0.050290361	3.544643891	3.93E-04
cluster 7	-0.696815579	0.075041761	-9.285703981	1.61E-20
cluster 8	0.277388403	0.093662032	2.961588568	3.06E-03
cluster 9	-1.155055839	0.051935689	-22.24011787	1.41E-109